A Numerical Investigation of The Energy Transfer of A Body Under Fluidelastic Galloping

By H.G.K.G Jayatunga

Doctor of Philosophy

Department of Mechanical Engineering
Monash University
October 2015

CONTENTS

CHAPTER 1

A REVIEW OF THE LITERATURE

1.1 Flow induced vibrations

1.2 Fluid-elastic galloping

Fluid-elastic galloping is one of the common observable flow-induced vibration on a slender body. This is because this phenomenon is most common in civil structures, such as buildings and iced-transmission lines, the term "aeroelastic galloping" is commonly used as the body is driven by wind. However, this mechanism can occur on a slender body immersed in any Newtonian fluid, provided that the conditions to sustain the galloping mechanism are satisfied. This work is based on a general Newtonian flow,thus the term " fluid-elastic galloping" is used throughout this thesis.

1.2.1 Excitation of galloping

Païdoussis et al. (2010) describe galloping as a "velocity dependent and damping controlled" phenomenon. Therefore, in order for a body to gallop, an initial excitation has to be given to that body. While this excitation is mainly caused by the force crated from vortex shedding, other fluid instabilities may contribute to this initial excitation. When a bluff body moves along the transverse direction of the fluid flow, it generates a force along the transverse direction. This force, also known as the induced lift and is a resultant of the fluid flow and the motion of the body. When this body is attached to a flexible system (i.e.
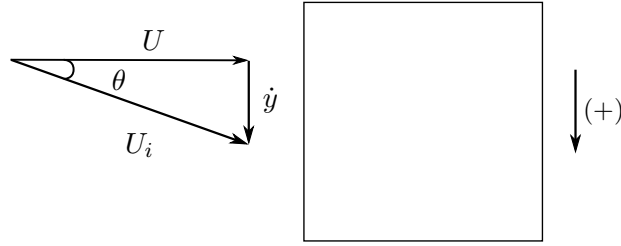
Figure 1.1: Induced angle of attack on the square prism due to the resultant of free-stream velocity of the fluid and transverse velocity of the body.

a system that can be modeled by a spring, mass and damper), the induced lift becomes the periodic forcing of the system. Galloping is sustained if the induced lift is in phase with the motion of the body. This could be explained further by using a square cross section as an example.

Figure 1.1 illustrates the motion of the body at a given instantaneous time.The induced angle of attack is formed on the square cross section as a result of the free stream velocity vector U and the transverse velocity vector of the body $\dot{y}$. Thus, a force is formed in phase with the motion of the body for the case of a square cross section. This mechanism could also be observed on other bodies which are prone to galloping. The sign convention in this figure (and generally used in this scope of research) states that downward direction is positive. Hence, the force generated on a body under the influence of galloping, could be also identified as a "negative lift".

1.2.2 Quasi-steady state theory

According Païdoussis et al. (2010),the initial studies by Glauert (1919) provided a criterion for galloping by considering the auto-rotation of a stalled aerofoil. As this phenomenon commonly occur in iced transmission lines, Den Hartog (1956) has provided a theoretical explanation for iced electric transmission lines.

The pioneering study that mathematically models galloping was conducted by Parkinson and Smith (1964). This model has been widely used in almost all subsequent studies on galloping. A weakly non-linear oscillator model was developed in that study to predict the response of the system. Essentially the quasi-steady assumption was made to develop this model. This assumes that the instantaneous induced lift force of the oscillating body

is equal to that of the lift force generated by the same body at the same induced angle of attack. For the quasi-steady assumption to be valid, the conditions below have to be satisfied.

- The velocity of the body does not change rapidly

- There is no interaction between vortex shedding and galloping

The second condition is satisfied by ensuring the vortex shedding frequency is much higher than the galloping frequency. The oscillator equation was solved using the Krylov and Bogoliubov method (Parkinson and Smith, 1964). Details of this method is not included in this thesis because this study uses numerical intergration instead. The results obtained form experiments, carried out at $Re = 2200$ and a mass ratio (m^*) around 1164 had a good agreement with the theoretical data which is shown in figure 1.2.

Quasi-steady state oscillator model

The equation of motion of transversely oscillating body is given by

$$m\ddot{y} + c\dot{y} + ky = F_y, \tag{1.1}$$

where the forcing term F_y is given by

$$F_y = \frac{1}{2}\rho U^2 \mathcal{A} C_y. \tag{1.2}$$

As explained previously, the quasi-steady assumption uses the stationary C_y data (which consists of both lift and drag components) for varying angles of attack as inputs to the oscillator equation. Parkinson and Smith (1964) used a 7th order odd interpolating polynomial to interpolate the C_y data. The order of the polynomial can be chosen arbitrarily depending on the study. For example Barrero-Gil et al. (2009, 2010) have used a 3rd order polynomial in order to simplify the analytical model. However, Ng et al. (2005) pointed out that a 7th order polynomial is sufficient as higher order polynomials do not provide significantly better result.

$$C_y(\theta) = a_1\left(\frac{\dot{y}}{U}\right) - a_3\left(\frac{\dot{y}}{U}\right)^3 + a_5\left(\frac{\dot{y}}{U}\right)^5 - a_7\left(\frac{\dot{y}}{U}\right)^7. \tag{1.3}$$
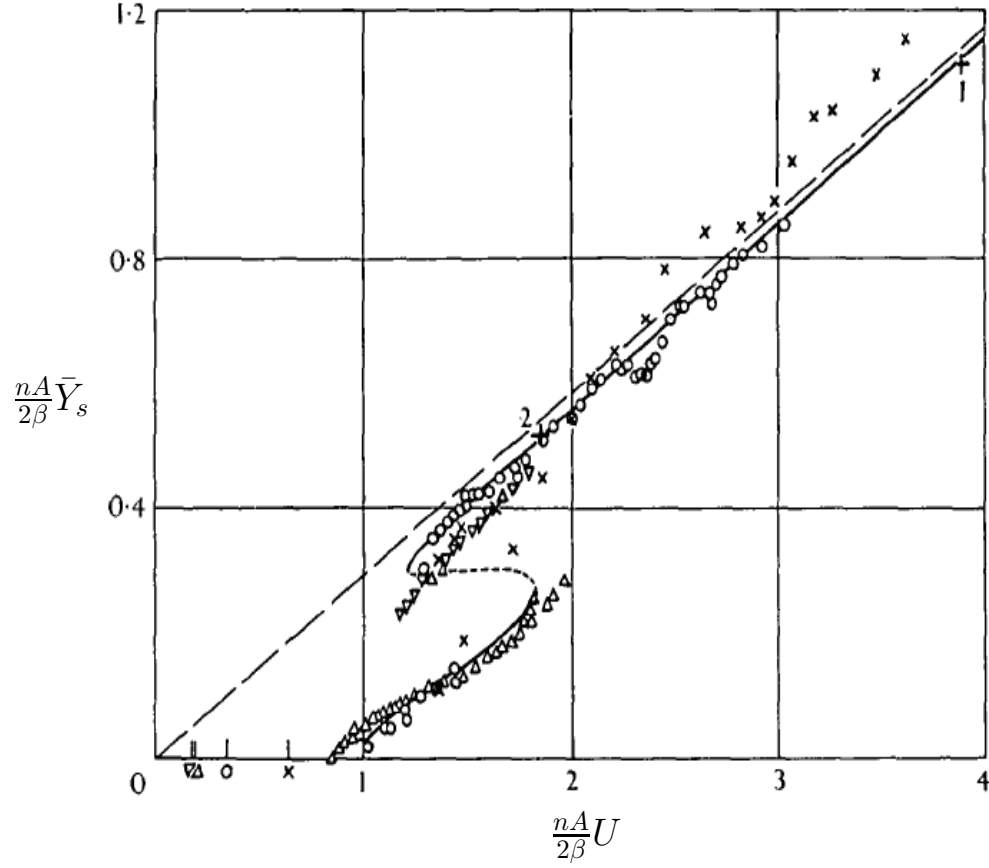
Figure 1.2: "Collapsed amplitude-velocity characteristic. Theory: —— stable limit cycle, --- unstable limit cycle. Experiment $\times$ $\beta = .00107$, $\circ$ $\beta = .00196$, $\triangle$ $\beta = .00364$, $\triangledown$ $\beta = .00372$, $+1$ $\beta = .0012$, $+2$ $\beta = .0032$ Reynolds numbers $4,000 - 20,000$ ". Figure extracted from Parkinson and Smith (1964). $\frac{nA}{2\beta}\bar{Y}_s$ is the dimensionless displacement amplitude parameter and $\frac{nA}{2\beta}U$ is the reduced velocity.

Therefore by substituting the forcing function to the oscillator equation (Eq:1.1) the Quasi-steady state (QSS) model could be obtained (Eq:1.4).

$$m\ddot{y}+c\dot{y}+ky=\frac{1}{2}\rho U^2 \mathcal{A}\left(a_1\left(\frac{\dot{y}}{U}\right)-a_3\left(\frac{\dot{y}}{U}\right)^3+a_5\left(\frac{\dot{y}}{U}\right)^5-a_7\left(\frac{\dot{y}}{U}\right)^7\right). \qquad (1.4)$$

As the current study is focused on the low Re region, it is a known fact that the vortex shedding will be correlated well and therefore provide a significant forcing. Joly et al. (2012) introduced an additional sinusoidal forcing function to the model in order to integrate the forcing by vortex shedding. By the addition of this forcing Joly et al. (2012) managed to obtain accurate predictions of the displacement amplitude even at low mass ratios, where the galloping is significantly suppressed by the vortex shedding to the point that it is no longer detectable. However, the strength or the amplitude of this sinusoidal forcing has to be tuned in an *ad hoc* manner, and it was not clear the relationship between this forcing with the other system parameters. Thus in the current study this forcing was not used.

Presence of hysteresis

Hysteresis could be observed in the amplitude data of Parkinson and Smith (1964). In contrast, the studies carried out by Barrero-Gil et al. (2009) and Joly et al. (2012) at much lower Reynolds numbers ($159 \leq Re \leq 200$), did not show any hysteresis. Luo et al. (2003) concluded that hysteresis was present due to the presence of an inflection point in the C_y curve at high Reynolds numbers (Parkinson and Smith (1964) data) which was not present at lower Reynolds numbers. It was further explained and demonstrated by Luo that the inflection point occurs due to the intermittent reattachment of the shear layer in certain angles at high Reynolds numbers.

Figure 1.2.2 shows the vorticity contours of a square cross section obtained at various points of the vortex shedding cycle, at $Re = 1000$, $\theta = 2°$ obtained from Luo et al. (2003). The points 7 and 11 show the intermittent shear layer reattachment which causes the hysteresis in the C_y vs. θ curve at high Reynolds numbers.
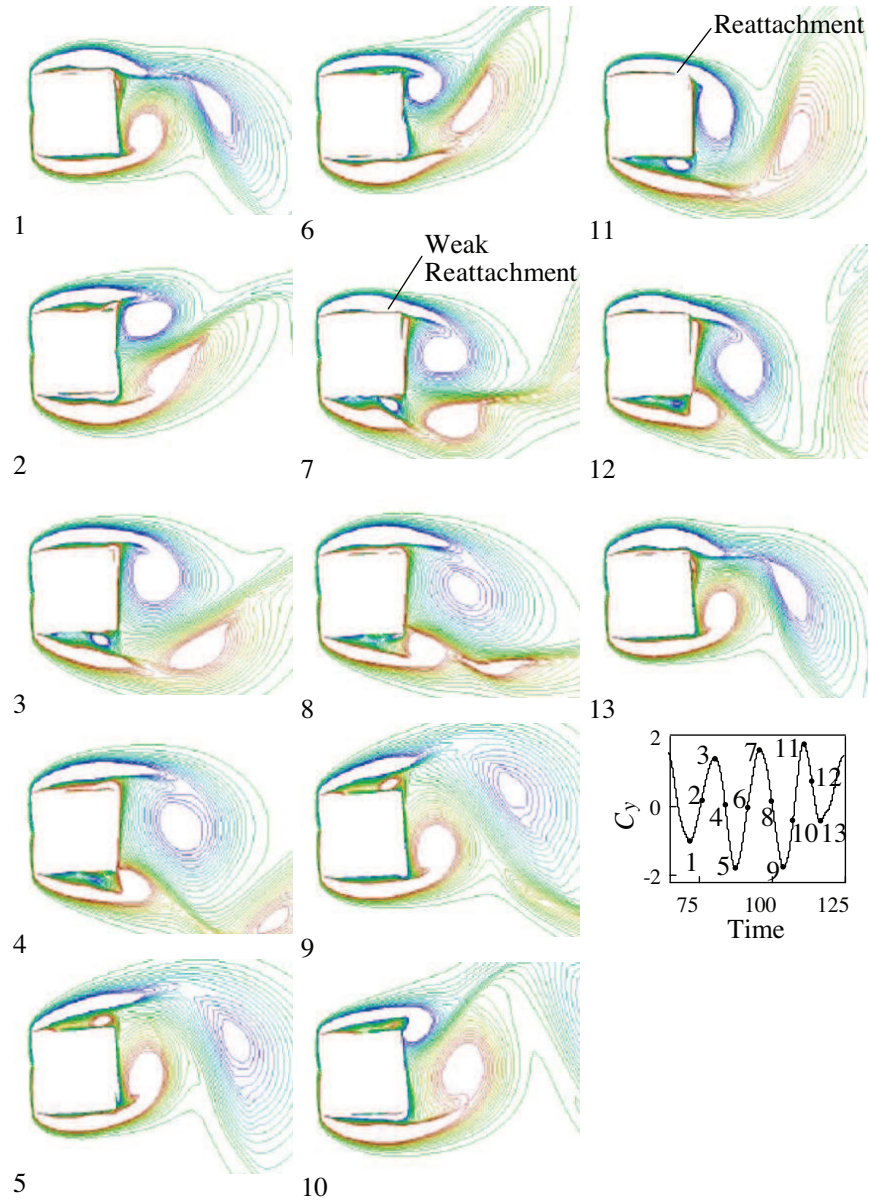
Figure 1.3: Vorticity contours of C_y and the corresponding time for $Re = 1000$, $\theta = 2°$ extracted from Luo et al. (2003). The intermittent shear level is visible in points 7 and 11

1.2.3   Induced force and the shear layers

The quasi-steady model has already been validated and re-validated by many studies (Parkinson and Smith, 1964; Barrero-Gil et al., 2009; Luo et al., 2003) and proven to model galloping. Since this model essentially assumes that the system is quasi-steady, the mean flow-field data of static body simulations at various angles of incidences could be used to analyse the behaviour of the instantaneous flow filed of a galloping system at the same instantaneous induced angle.
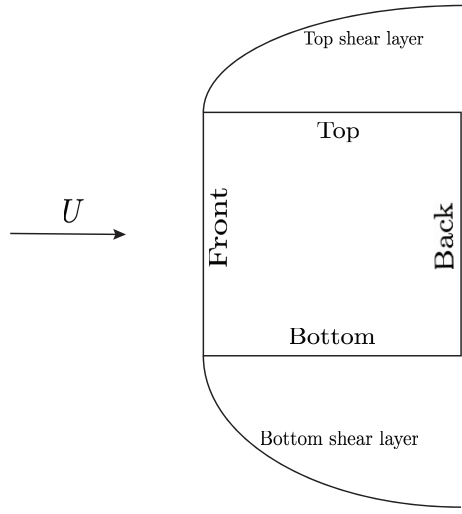
Figure 1.4: Illustration of the top and bottom shear layers

Païdoussis et al. (2010); Parkinson and Smith (1964); Barrero-Gil et al. (2010) and many other published literature states that a system which sustains galloping should satisfy the condition of being $\partial C_y/\partial\theta > 0$. The mean positive induced lift (C_y) occurs due to the unbalanced pressure distribution of the top and bottom sides of the afterbody of the cross section (refer figure 1.4) when a small transverse velocity is given (Parkinson, 1989). This pressure difference of the afterbody is a result of the relative proximity of the top and bottom shear layers (illustrated in figure 1.4) to the respective sides of the body.

Vorticity contour plots of a static square cross section at various incidence angles shown in figure 1.5 clearly shows the behaviour of the shear layers at either sides of the body. Data are presented for three key incidence angles $2°, 4°$ and $6°$. In comparison with figure 3.1 it could be identified as the points which lies on regions where C_y initially increases, C_y

(a)   (b)   (c)
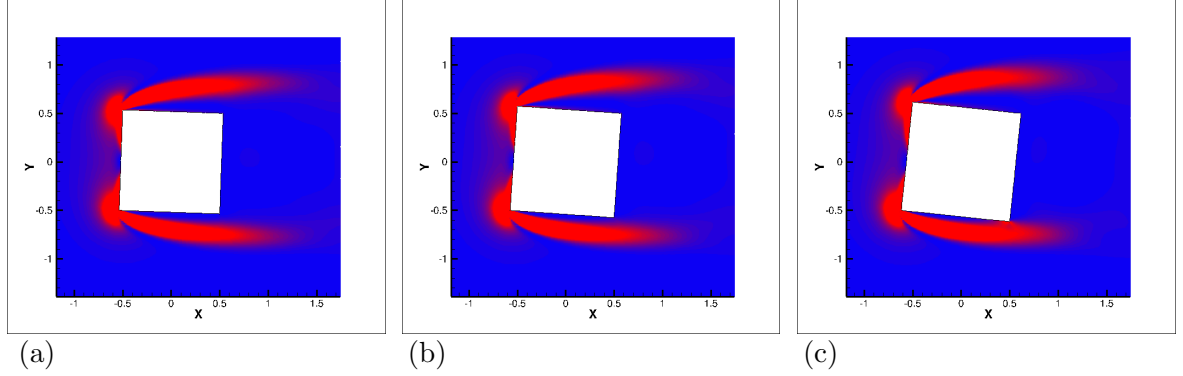
Figure 1.5: Shear strain rate magnitude contours of time averaged flow field on a stationary square section at $Re = 200$ at different incidence angles. (a) $2°$ (C_y increases),(b) $4°$ (C_y peaks) and (c) $6°$ (C_y decreases). The bottom shear layer comes closer to the bottom wall and reattaches as the angle of incidence increases.

maximises and C_y decreases.

As the angle of incidence (θ)increases clockwise from $2° - 6°$, it could be clearly observed in figure 1.5 that the bottom shear layer comes closer to the bottom wall of the body compared to the top shear layer. The shear layer nearer to the body creates higher suction compared to the shear layer at the opposite side. This pressure imbalance between the top and bottom sides of the body creates a downward force which with the sign convention introduced in figure 1.1 is positive. As the angle is further increased to $\theta = 4°$, the bottom shear layer becomes closer and therefore the pressure difference becomes greater leading to a higher C_y. The induced lift force C_y, becomes maximum when the shear layer near to the wall reattaches at the trailing edge. As θ is further increased at $\theta = 4°$ (figure 1.5 (b)), the bubble in the bottom shear layer shrinks in size resulting the reduction of the pressure imbalance of the top and bottom surface leading to the reduction in C_y. This theory has been discussed in Parkinson (1989). The variation of C_y vs θ is presented in figure 3.1. As the body is connected to an oscillatory system (discussed in section 1.2.1), this shear layer behaviour also harmonizes with the cyclic behaviour of the system providing the driving force to the system so that the motion of galloping is sustained for triangular cross section.

1.2.4 Frequency response
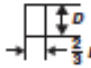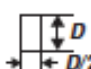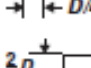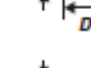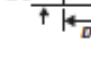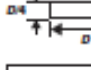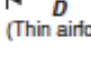
It is clear that the cyclic motion of the shear layer harmonize with the mechanical system. Therefore, the frequency response should be then, the natural frequency of the system ω_n (Païdoussis et al., 2010). This is significantly different from the VIV mechanism, where the primary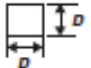 frequency comes from the periodic forcing of the vortex shedding. Hence, in the QSS model the natural frequency of the system could be identified as the frequency of oscillations. However, it should be noted that this is valid on the regimes where the conditions discussed in section 1.2.2 are satisfied.

The experimental studies carried by Bouclin (1977) concluded at high reduced velocities with large inertia, the motion of the cylinder controls the frequency of the system rather than the vortex shedding. The structural damping has no effect provided that it is small. He also concluded that as the inertia and the reduced velocity gets lower, there is some interaction between vortex shedding and galloping. And at this region the frequency is mainly governed by the vortex shedding.

1.2.5 Fluid mechanics governing the galloping response

As discussed in subsection 1.2.3 the driving force of a galloping system is the asymmetrical placement of the shear layers at either sides of the body. In consequence, it is clear that a significant afterbody is needed for the shear layer interaction to sustain galloping. Parkinson (1974, 1989) and Bearman et al. (1987) have discussed well the importance of the length and the shape for galling in their reviews. It is also highlighted in Parkinson (1974) that the most important physical parameters for galloping are the size relative to the characteristic hight and the shape of the afterbody. Manipulating the shape of the afterbody and thereby, manipulating the shear layer interactions with the body, gives the ability to control the galloping response. Thus, due to this reason work has been carried out on the response of galloping of different cross sectional shapes.

Blevins (1990) provided a good comparison of the shapes which are prone to galloping based on the work by Parkinson and Brooks (1961), Nakamura and Mizota (1975) and Nakamura and Tomonari (1977). The reproduction of Blevins's data could be found in Païdoussis et al. (2010) presented in figure 1.6.

Section	h/d	$\partial C_{F_y}/\partial \alpha$ Smooth flow	$\partial C_{F_y}/\partial \alpha$ Turbulent flow[b]	Reynolds number
	1	3.0	3.5	10^5
	3/2	0.	−0.7	10^5
	2	−0.5	0.2	10^5
	4	−0.15	0.	10^5
	2/3	1.3	1.2	6.6×10^4
	1/2	2.8	−2.0	3.3×10^4
	1/4	−10.	–	$2 \times 10^3 - 2 \times 10^4$
(Thin airfoil)	–[c]	−6.3	−6.3	$> 10^3$
	–	−6.3	−6.3	$> 10^3$
	–	−0.1	0.	6.6×10^4
	–	−0.5	2.9	5.1×10^4
	–	0.66	–	7.5×10^4

[a] α is in radians; flow is left to right. $\partial C_{F_y}/\partial \alpha = -\partial C_L/\partial \alpha - C_D$, with C_{F_y} based on the dimension D, so that $\partial C_{F_y}/\partial \alpha > 0$ for galloping.
[b] Approximately 10% turbulence.
[c] Inappropriate to use h/d.

Figure 1.6: "The transverse force coefficient for various sections in steady smooth or turbulent flow (after Blevins (1990))" obtained from Païdoussis et al. (2010)

Naudascher and Wang (1993), Ruscheweyh et al. (1996), Deniz (1997) and Weaver and Veljkovic (2005) are some of the work done on different cross sectional shapes. Alonso et al. (2009) carried out wind tunnel tests on biconvex and rhomboidal cross sections. This study concluded that the galloping stability is dependent on the angle of attack. The aspect ratios where galloping is sustained in these cross sections were identified. Studies were further carried out by Alonso for elliptical cross sections (Alonso et al., 2010) which concluded that galloping is Reynolds number dependent for elliptical cross sections. The study triangular cross sections carried out by (Alonso et al., 2005) isolated the angle of attacks where galloping is stained. The regions of stability for galloping at different angles of attack and the static force coefficients are presented in these studies with regards to the cross section involved. Luo et al. (1994) carried out an interesting study where the influence of the afterbody on galloping was investigated. The sides of a square section was chamfered gradually delaying the shear layer re-attachment, and two trapezoidal cross sections and one isosceles triangle was obtained. The C_y vs. θ plots revealed that the maximum value of C_y increased as the chamfering angle increased (i.e when the cross section was transformed from a square to a isosceles triangle). Anther interesting observation was that the incident angle where maximum C_y occurred increased as the chamfering angle increased. Delaying shear layer reattachment leads to higher C_y at higher induced angles which leads to higher induced velocities. This fact is beneficial for energy harvesting because as shown in equation 2.2 power is a function of both F_y and the velocity of the body.

1.2.6 Galloping as a mechanism of energy harvesting

The focus on fluid-elastic galloping in the past was on understanding and developing methods to suppress it, due to the adverse effects on civil structures. However, recently, the focus of research has been redirected to develop mechanisms to excite galloping rather than suppressing it. This is due to the recent demand for alternative energy sources with minimal environmental impact. Thus, this demand for alternate energy has lead researchers to develop ways of extracting useful energy from flow induced vibrations.

Bernitsas and his group in the University of Michigan have made significant progress on using VIV as potential candidate for energy extraction. Bernitsas et al. (2008) introduced the concept of using VIV as a mode of energy extraction.The group have developed a device

called VIVACE converter based on this concept. The work has been further expanded to focus on various aspects (such as Reynolds number effects, damping effects etc.) in Bernitsas et al. (2009); Raghavan et al. (2009); Raghavan and Bernitsas (2011); Lee et al. (2011). This group has studied extensively on the effect of the mechanical parameters, the Reynolds number effects and the bottom boundary conditions of the VIVACE converter, in order to obtain efficient energy output using VIV as an energy harvesting mechanism.

In contrast, the research carried out investigating the possibility of energy harvesting using fluid-elastic galloping is quite limited. Barrero-Gil et al. (2010) conducted the pioneering study on energy harvesting using fluid-elastic galloping. The key consideration to investigate on galloping in this study was that unlike VIV fluid-elastic galloping is not dependent on a synchronisation or a "lock-in" mechanism. Therefore, it could operate on a wide spectrum of frequencies giving fluid-elastic galloping an advantage over VIV as a mechanism of energy harvesting. Vicente-Ludlam et al. (2014) showed that there is a link between the optimal electrical load resistance and the flow speed. However, it was identified that the understanding is primary and therefore step-by-step research has to be conducted in order to properly understand the link between energy transfer in the galloping mechanism.

1.2.7 Review summery and Objectives

It is clear that more investigations should be carried out on energy transfer of a galloping system, particularly to develop efficient energy harvesting system. More fundamental research is needed to explore the underpinning effects of mechanical and fluid dynamic parameters influencing the energy transfer of a galloping system to fill the gaps of the existing knowledge base. Thus, objectives of the current research were formulated in order to address these research gaps.

Thus, this study was divided into two phases and objectives were defined as follows.

Phase 1: Understand the governing mechanical parameters of the system and isolate regions where a good power transfer could be obtained

Païdoussis et al. (2010) describes galloping as a "velocity dependent damping controlled phenomenon". Yet, so far the scaling parameters used in studies are the traditional VIV

parameters which are the damping ratio ζ and the reduced velocity U^* (Barrero-Gil et al., 2010) which has a embedded frequency component. Thus following objectives were defined for this phase

- Formulate a new set of scaling parameters bates on the natural time-scales of the system.

- Investigate the influence of these parameters on mean power transfer.

- Isolate the regions where high power transfer could be obtained.

- Investigate the relationship between these new scaling parameters and the frequency response of the system.

Phase 2: Understand the fluid mechanics of the system and optimise and control these mechanics to obtain a higher power transfer

Luo et al. (1994) showed that delaying shear layer reattachment could lead to higher peak F_y at higher induced angles and therefore higher transverse velocities. Thus, from equation 2.1, it could be hypothesised that a higher mean power could be obtained by delaying the shear layer reattachment. Hence, the following objectives were defined for phase 2.

- Obtain QSS power data by systematically delaying the shear layer and investigate the influence on power.

- Identify the relationship of involved fluid mechanics and the mean power output through analysis of the flow-filed.

- Provide design considerations for a galloping energy extraction system through control of the shear layers.

CHAPTER 2

METHODOLOGY AND VALIDATION

2.1 Introduction

An overview of the modeling and the computational methods used in this study are presented in this chapter. This study uses well established techniques to model and study fluid elastic galloping. Therefore, only a brief overview is provided together with relevant references where the development and vigorous validation has been presented.

This chapter is presented as follows. The equations used to model the system are presented and discussed. Next, a brief discussion of the techniques used for direct numerical simulations are presented followed by the problem formulation and the discussion of the parameters used. Finally, validation data are presented and discussed to demonstrate the accuracy of the direct numerical simulations.

2.1.1 Parameters used

The findings in this study are presented in two categories i.e. high and low Reynolds numbers, so as to study the system at laminar and turbulent flow regimes. One of the main objectives in this study was to capture the flow physics accurately using direct numerical simulations. Hence, major portion of the study was carried out in the laminar range where the flow is laminar and two directional. Although a majority of the study is focused on low Reynolds number regime, some results were presented using inputs from published data at high Reynolds numbers to provide a comparison between high and low Reynolds number

cases. $Re = 200$ was defined as the "low" Reynolds number and $Re = 22300$ was defined as the high Reynolds number in this study. Studies by Tong et al. (2008) and Sheard et al. (2009) reveal that the approximate value of 3-dimensional transition of the wake for a square cross section is $Re = 160$ and therefore, $Re = 200$ was selected to represent the low Reynolds number regime, also considering the fact that other numerical studies in the laminar regime have used this value of Reynolds number (Robertson et al., 2003; Joly et al., 2012). All these published data have used a square cross section as the body of oscillation. Since the basic cross section used in this study is square, the same flow regimes of the these published data were used.

In the high Reynolds number case, the chosen Reynolds number matches the pioneering study of galloping Parkinson and Smith (1964), from which the stationary aerodynamic data was obtained as imput to the QSS model. For the high Re tests, predictions of power output at $Re = 22300$ were obtained using the coefficients of the C_y vs. θ curve from Parkinson and Smith (1964) as inputs to the QSS model. Aerodynamic data (i.e. C_y data) from direct numerical simulations at low Reynold number of stationary cases at different angles of attack are used as inputs to the QSS model at the low Reynolds number regime.

Stationary C_y data at different angles of attack is used as inputs to the QSS model, were obtained for the low Reynolds number regime using direct numerical simulations. The average power was obtained by using equation 2.1, and the averaging was done over no less than 20 galloping periods. The mass ratio m^* was kept at 1163 for $Re = 22300$ (Similar to Parkinson and Smith (1964)). The parameters used at the low Reynolds number cases are $m^* = 20$ for Re=200 and $U^* \geq 40$. These were similar to the parameters used in previous studies (Robertson et al., 2003; Joly et al., 2012). These parameters were used throughout this study unless specified otherwise.

2.2 Quasi-steady model

The quasi-steady state model discussed in section 1.2.2 was used to obtain oscillator response data. The quasi-steady state model has proven its ability to obtain accurate galloping response data (as also discussed in section 1.2.2). Therefore, a large number of cases can be modelled in small amount of computational time. The oscillator equation consists

of spring, mass and damper oscillator expression with a 7th order interpolation polynomial as the forcing function (equation 1.4), obtained from a curve fit of aerodynamic data (i.e. C_y as a function of the incidence angle).

Solving the quasi-steady state equation

The quasi-steady model being an ordinary differential equation could be solved using different solving methods. Some of the techniques include limit cycle oscillations, harmonic balance, cell mapping and numerical integration. Vio et al. (2007) showed that numerical integration provides accurate data. A fourth-order Runge-Kutta ODE solving scheme was used in solving the quasi-steady state oscillator equation. The built in 'ode45' function in MATLAB was used primarily to solve the QSS equation while in some cases 'ode15s' function was used when the equation became more stiff.

2.3 Calculation of average power

The ideal potential amount of harvested power output could be represented as the dissipated power due to mechanical damping before losses in any power take-off system are included. Thus the mean power output could be expressed as

$$P_m = \frac{1}{T} \int_0^T (c\dot{y})\dot{y}dt, \tag{2.1}$$

where T is the period of integration and c is the mechanical damping constant.

The work done on the body by the fluid is equal to this quantity, defined as

$$P_m = \frac{1}{T} \int_0^T F_y \dot{y}dt, \tag{2.2}$$

where F_y is the transverse (lift) force.

The two definitions of the mean power provide two vital interpretations of power transfer. Equation 2.1 shows that the power is proportional to the mechanical damping and the magnitude of the transverse velocity. At first glance one may assume that the power could be increased by increasing damping. In a practical power extraction device, the significant component of damping would be due to the electrical generator and therefore, an increase in damping would be due to the increase of the load or in other words the electrical resistance. Yet this perception of damping is not quite accurate as very high damping would

result in reducing the velocity amplitude which then, would not result in a higher energy output according to equation 2.1. In consequence, a balance needs to be obtained where the damping is high, but not to the extent that it will adversely result by overly suppressing the motion of the body.

On the other hand, equation 2.2 shows that a higher power is attained during situations where the transverse force F_y and the transverse velocity are in phase. Hence, a simple increase in the magnitude of the force or the velocity is not satisfactory to attain a higher power transfer. A higher power output could be obtained when there is a smaller phase difference between the force and the velocity.

2.4 Direct numerical simulations (DNS)

Direct numerical simulations were employed to obtain the stationary data to be used as inputs to the QSS model and to obtain fluid-structure interaction (FSI) predictions to be compared with the QSS model at low Reynolds numbers. A high-order in-house build spectral element which simulates two-dimensional laminar flows was used to obtain the DNS data.

To obtain DNS results an in-house build code was used. This code essentially solves the Navier-Stokes equations in an accelerated reference frame. A three-step time-splitting scheme also known as a fractional step method was used for temporal discretisation. A predictor-corrector method was used for the FSI data where an elastically mounted body was involved. A description of the spectral element method in general can be found in Karniadakis and Sherwin (2005). This code has been very well validated in a variety of fluid-structure interaction problems similar to that studied in the current study (Leontini et al., 2007; Griffith et al., 2011; Leontini et al., 2011; Leontini and Thompson, 2013). An overview of the algorithm is presented in the following subsections which is described in detail by Leontini (2007).

2.4.1 Governing equations

In this study, the following key assumptions were made to carry out the direct numerical simulations.

To formulate the differential equations to an infinitesimally small fluid section, the fluid was assumed to be a continuum. This assumption is valid for all macro flows as is the case in this study.

Next, to avoid the modelling acoustic wave propagation, it was assumed that the density of the fluid is constant. The fluid is incompressible. This particular assumption is usually valid for Mach numbers (ratio of the speed of sound to the speed of fluid flow) less than 0.3.

Finally, the fluid was assumed to be an Newtonian fluid, which means that the shear stress is directly proportional to the strain rate.The assumptions used are quite standard and further information could be found in White (1999).

The Navier-Stokes equations are the equations which governs a Newtonian, incompressible fluid.

$$\frac{\partial \mathbf{u}}{\partial t} + (\mathbf{u} \cdot \nabla)\mathbf{u} \; = -\frac{\nabla p_f}{\rho} + \frac{\mu_v}{\rho}(\nabla^2 \mathbf{u}) \; , \tag{2.3}$$

and continuity,

$$\nabla \cdot \mathbf{u} = 0 \; . \tag{2.4}$$

The velocity vector filed is represented by $\mathbf{u}$, time by t, the pressure field by p_f fluid density by ρ and the dynamic by μ_v. In the Navier-Stokes equation (2.3) the left hand side represents the inertial forces and the right hand side represents the pressure forces. The net mass flux into the fluid element is specified to be zero by the continuity equation.

These equations are generalised by non-dimensionalisation. In the case of bluff body wake flows, the equations are non-dimensionalised by using the characteristic length of the body i.e the frontal projected hight D, and the free-stream velocity U.

For cases investigating fluid structure interactions the equations are modified to be solved in an accelerated reference frame. The frame of reference is attached to the cylinder. Therefore, an extra term is added to the Navier-stokes equations which represents the acceleration of the cylinder. Thus, the equations could be written as,

$$\frac{\partial \mathbf{V}}{\partial \tau} = -\nabla P + \frac{1}{Re}(\nabla^2 \mathbf{V}) - (\mathbf{V} \cdot \nabla)\mathbf{V} + \frac{d\mathbf{V}_{cyl}}{d\tau} \; , \tag{2.5}$$

$$\nabla \cdot \mathbf{V} = 0 \; . \tag{2.6}$$

The non dimensional terms are defined s follows: $\mathbf{V} = \mathbf{u}/U$, $\tau = tU/D$, $P = p_f/(\rho U^2)$, $Re = \rho U D/(\mu_v)$, $\mathbf{V}_{cyl} = \mathbf{v}_{cyl}/U$, and $\mathbf{v}_{cyl}$ being the velocity of the cylinder. $\frac{\mathrm{d}\mathbf{V}_{cyl}}{\mathrm{d}\tau}$, represents acceleration of the cylinder.

The Navier-Stokes equations are coupled with the oscillator differential equation

$$\frac{\ddot{y}_{cyl}}{D} + 2\zeta\sqrt{k^*}\frac{\dot{y}_{cyl}}{D} + k^*\frac{y_{cyl}}{D} = \frac{\pi}{2}\frac{C_L}{m^*} \; , \tag{2.7}$$

Where ζ is the damping ratio, $k^* = kD^2/mU^2$ and $C_L = F_{lift}/(0.5\rho U^2 D)$. The lift coefficient per unit length of the body is C_L, the transverse displacement of the cylinder is given by y_{cyl}, the characteristic length scale of the body is D, k is the spring constant and the mass per unit length of the body is represented by m. The general form of this linear oscillator equation could be found in books such as Naudascher and Rockwell (1994). The final form of the coefficients were constructed by non-dimensionalising the general linear oscillator equation.

2.4.2 Temporal discretisation: Time-splitting

The problem was discretised in order to solve equations 2.5, 2.6 and 2.7 in both space and time. A three-step time splitting method was used for the temporal discretisation. This scheme also known as the fractional step method, was used to separately integrate the terms in the right hand side of the Navier-Stokes equation (Karniadakis and Sherwin, 2005). The overall integration of one time-step is split into three substeps. An approximate solution of the Navier-Stokes equation is gained by this scheme.

The cylinder acceleration is integrated through the whole time step in order to obtain an initial approximation of the intermediate velocity filed. This velocity filed is used as the starting condition. The pressure is integrated using this starting condition. A secondary intermediate velocity filed is obtained as a result of the pressure integration substep. This secondary velocity filed is then used as the starting condition for the integration of the diffusion term which results in the final velocity filed.

The three semi-discretised substep equations are as follows:

$$\mathbf{V}^* - \mathbf{V}^{(n)} - \Delta\mathbf{V}_{cyl} = -\int_\tau^{\tau+\Delta\tau}(\mathbf{V}\cdot\nabla)\mathbf{V}\mathrm{d}\tau \tag{2.8}$$

$$\mathbf{V}^{**} - \mathbf{V}^* = -\int_{\tau}^{\tau+\Delta\tau} \nabla P \mathrm{d}\tau \qquad (2.9)$$

$$\mathbf{V}^{(n+1)} - \mathbf{V}^{**} = \frac{1}{Re} \int_{\tau}^{\tau+\Delta\tau} \nabla^2 \mathbf{V} \mathrm{d}\tau, \qquad (2.10)$$

The current time step is represented by n and the intermediate velocity fields at the end of the convection and pressure substeps are $\mathbf{V}^*$ and $\mathbf{V}^{**}$ respectively. The change in the body over a time step is given by $\Delta\mathbf{V}_{cyl} = \int_{\tau}^{\tau+\Delta\tau} \frac{\mathrm{d}\mathbf{V}_{cyl}}{\mathrm{d}\tau} \mathrm{d}\tau$.

The addition of these three substep equations reduces to the integrated form of the Navier-Stokes equation in equation 2.5.

Integration of the substep equations

The integration methods of the pressure, convection and diffusion substeps are presented in this subsection.

The convection substep

As the system involves free oscillation, a coupling between the oscillation equation (equation 2.7) and the Navier-Stokes equations had to be employed. As a result, the cylinder dynamics had to be solved at each time-step.

An iterative predictor-corrector scheme was employed to obtain the solution of the coupled equations. The initial step being the "predictor" step was obtaining approximations for all the quantities involved in the integration. A quadratic extrapolation was used to obtain an initial estimate of $\Delta\mathbf{V}_{cyl}$ from three previous time step values of $\mathbf{V}_{cyl}$. Therefore, a non-dynamical approximation could be obtained.

$$\mathbf{V}_{cyl}^{(n+1)\dagger} = 3\mathbf{V}_{cyl}^{(n)} - 3\mathbf{V}_{cyl}^{(n-1)} + \mathbf{V}_{cyl}^{(n-2)} , \qquad (2.11)$$

The dagger ($\dagger$) indicates that the value is an initial approximation eg. $\mathbf{V}_{cyl}^{(n+1)\dagger}$. Thus, $\Delta\mathbf{V}_{cyl}^{\dagger}$ was obtained by a simple subtraction of the value at the current time step.

The approximated position of the cylinder at the next time step could be obtained by carrying out an integration of the cylinder velocity over the time step. A third-order Adams-Moulton method was used to perform the integration. Therefore, the final equation describing the position of the body is given by,

$$\frac{y_{cyl}^{(n+1)\dagger} - y_{cyl}^{(n)}}{\Delta\tau} = \frac{1}{12}(5\mathbf{V}_{cyl}^{(n+1)\dagger} + 8\mathbf{V}_{cyl}^{(n)} - \quad\quad (2.12)$$

The transverse displacement of the cylinder is denoted by y_{cyl}.

An offset is present between the cylinder velocity and cylinder position. The velocity of the cylinder is in advance by half a time-step of the position of the cylinder, i.e. $\mathbf{V}_{cyl}^{(n+1)}$ is half a time step is in advance of $y_{cyl}^{(n+1)}$. However, both the cylinder positions and the velocities are located at the same discrete times.

In order to obtain an approximation for $\mathbf{V}^*$, a solution was obtained for equation 2.8 using the previous approximated quantities.

By using a third-order Adams-Bashforth scheme and incorporating the approximation of equation 2.11 for $\Delta\mathbf{V}_{cyl}^{\dagger}$ the first approximation for $\mathbf{V}^*$ was obtained using the equation,

$$\frac{\mathbf{V}^* - \mathbf{V}^{(n)} - \Delta\mathbf{V}_{cyl}^{\dagger}}{\Delta\tau} = \frac{1}{12}(23\mathbf{N}(\mathbf{V})^{(n)} - 16\mathbf{N}(\mathbf{V})^{(n-1)} + 5\mathbf{N}(\mathbf{V})^{(n-2)}) \ . \quad\quad (2.13)$$

The explicit integration method was only used for the first approximation and for the subsequent iterations semi-implicit method was used for $\mathbf{V}^*$.

This step was followed by solving the remaining substep equations in order to obtain an approximation for $\mathbf{V}^{(n+1)\dagger}$, and then the "predictor" portion of the predictor-corrector method was completed.

The cylinder velocity approximation $\mathbf{V}_{cyl}^{\dagger}$, was updated commencing the "corrector" cycle of the predictor-corrector method. This was carried out using a third-order integration scheme.

$$\frac{\mathbf{V}_{cyl}^{(n+1)\dagger} - \mathbf{V}_{cyl}^{(n)}}{\Delta\tau} = \frac{1}{24}(25\ddot{y}_{cyl}^{(n+1)} - 2\ddot{y}_{cyl}^{(n)} + \ddot{y}_{cyl}^{(n-1)}) \ . \quad\quad (2.14)$$

$\Delta\mathbf{V}_{cyl}^{\dagger}$ was updated using the recalculated value of $\mathbf{V}_{cyl}^{(n+1)\dagger}$. The velocity was integrated over a time step in order to obtain the position of the cylinder. For the first correction cycle a third order Adams-Moulton method was used which completed the first iteration of the predictor-corrector method.

$$\frac{y^{(n+1)\dagger} - y^{(n)}}{\Delta\tau} = \frac{1}{12}(5\mathbf{V}_{cyl}^{(n+1)\dagger} + 8\mathbf{V}_{cyl}^{(n)} - \mathbf{V}_{cyl}^{(n-1)}) \ , \quad\quad (2.15)$$

Slight modifications were employed to the subsequent iterations in order to improve numerical stability. However, the iterations proceeded in a similar manner. As the approximations for $\Delta\mathbf{V}^{\dagger}_{cyl}$ and $\mathbf{V}^{(n+1)\dagger}$ were available, further correction steps were carried ou using third-order Adams-Moulton scheme .

$$\frac{\mathbf{V}^{*} - \mathbf{V}^{(n)} - \Delta\mathbf{V}^{\dagger}_{cyl}}{\Delta\tau} = \frac{1}{12}(5\mathbf{N}(\mathbf{V})^{(n+1)\dagger} + 8\mathbf{N}(\mathbf{V})^{(n)} - \mathbf{N}(\mathbf{V})^{(n-1)}) \ . \qquad (2.16)$$

The two remaining substeps were then solved to obtain a new approximation of $\mathbf{V}^{(n+1)\dagger}$.

The first correction step was carried out by employing 2.14 to obtain a second estimate for the velocity of the cylinder $\mathbf{V}^{(n+1)\ddagger}_{cyl}$. A relaxation equation (equation 2.17) was used for the velocity of the cylinder prior to using equation 2.15 since the equations were quite stiff.

$$\mathbf{V}^{(n+1)\prime}_{cyl} = \mathbf{V}^{(n+1)\dagger}_{cyl} + \epsilon(\mathbf{V}^{(n+1)\ddagger}_{cyl} - \mathbf{V}^{(n+1)\dagger}_{cyl}) \ , \qquad (2.17)$$

$\mathbf{V}^{(n+1)\ddagger}_{cyl}$ and $\mathbf{V}^{(n+1)\dagger}_{cyl}$ represent the most current and previous approximations respectively. The under relaxation parameter is represented by ϵ which controls the proportion of the correction which is considered in each iteration. The final approximation at the end of the relaxation process is represented by $\mathbf{V}^{(n+1)\prime}_{cyl}$ and was used in equation 2.15 for completing the correction cycle and hence, the iteration.

A convergence error criteria was specified until which the iteration was continued. The lift force of the cylinder, the velocity of the cylinder and the fluid velocity should all converge to the required convergence criteria. A series of convergence studies were carried out in order to obtain the convergence criteria (Pregnalato, 2003). The solution converged typically within $3 - 4$ iterations and the iteration count exceeded 10 in very rare cases.

The procedure to obtain the solution for $\mathbf{V}^{*}$ (velocity filed at the end of the convection subsetep) in a nutshell is as follows. A predictor-corrector method was employed, where the primary predictor cycle was first employed. This was followed by obtaining an approximation for $\Delta\mathbf{V}_{cyl}$ which was calculated using equation 2.11. From this approximation $(\Delta\mathbf{V}_{cyl})$ the position of the cylinder was approximated using equation 2.12.

Next, using an explicit Adams-Bashforth scheme, an approximation was obtained for $\mathbf{V}^{*}$ by solving the substep equation (equation 2.13). The predictor cycle was completed by solving the remaining substep equations to arrive at the first approximation of $\mathbf{V}^{(n+1)}$.

Then, the primary corrector step was initiated by calculating the forces of the body from the current approximation of $\mathbf{V}^{(n+1)}$. Using these forces together with the current approximations of the velocity and the displacement of the body and the equation of motion of the body (eq:2.7) an approximation for the acceleration of the cylinder at the end of the timestep was obtained. By integrating this acceleration over the timestep using equation 2.14 the corrected approximation of $\Delta \mathbf{V}_{cyl}$ was obtained. Using equation 2.15 the corrected approximation for $y_{cyl}^{(n+1)}$ was obtained by integrating the velocity over a timestep and using the recent value of $\Delta \mathbf{V}_{cyl}$. The primary corrector step and the primary iteration was completed once this step was completed. All the remaining iterations were carried out in a similar manner with an under relaxation presented in equation 2.17.

The pressure substep

The pressure equation was solved in two parts in order to find solutions to the two unknowns i.e. the pressure filed na d the velocity filed at the end of the timestep.

The integration of the pressure substep was initiated by formulating equation 2.9 in terms of a second-order Adams-Moulton scheme which gives,

$$\frac{\mathbf{V}^{**} - \mathbf{V}^*}{\Delta \tau} = -\frac{1}{2}(\nabla P^{(n+1)} + \nabla P^{(n)}) \ . \tag{2.18}$$

The equation was further reduced by considering that the RHS is equal to $\nabla P^{(n+1/2)}$. The divergence portion of equation 2.18 was taken. Using equation 2.6, continuity was applied to the velocity filed which resulted the pressure filed having a Poisson equation of the form of

$$\nabla^2 P^{(n+\frac{1}{2})} = \frac{1}{\Delta \tau}\nabla \cdot \mathbf{V}^* \ . \tag{2.19}$$

This equation could be solved at the middle of the timestep for the pressure filed. Therefore, this pressure filed could then be back-substituted to equation 2.18, together with the simplified RHS, to solve for the velocity filed $\mathbf{V}^{**}$, at the end of the substep.

The diffusion substep

A numerical stability of the solution scheme has to be considered for the diffusion substep although the equation for diffusion is linear. Therefore, the Crank-Nicholson scheme or the

second order Adams-Moulton scheme which is a semi-implicit scheme and unconditionally numerically stable is employed. Thus this formulates the final equation (eq 2.10) of the time splitting scheme as,

$$\frac{\mathbf{V}^{(n+1)} - \mathbf{V}^{**}}{\Delta \tau} = \frac{1}{2Re}(\nabla^2 \mathbf{V}^{(n+1)} + \nabla^2 \mathbf{V}^{(n)}) \ . \tag{2.20}$$

The integration over the timestep is obtained from the solution of this equation for $\mathbf{V}^{(n+1)}$, thus completing the time splitting scheme.

Spatial discretisation:Spectral element method

The spacial discretisation was done using a nodal based spectral-element method. This method is a member of the finite-element class. The computational domain is separated into a series of macro elements and then a continuous solution is obtained over each element. Mesh refinement can be done in the areas where high gradients are experienced, which is also known as h-refinement. It was necessary that all elements to be quadrilateral. Yet, the elements were not restricted from having curved sides.

The calculation of the residual $\mathbf{R}$ initiates the solution process. All the terms of the governing equations (the Navier-Stokes equation eq 2.5) were moved to the LHS. Thus, the resulting expression is,

$$\frac{\partial \mathbf{V}}{\partial \tau} + \nabla P - \frac{1}{Re}(\nabla^2 \mathbf{V}) + (\mathbf{V}.\nabla)\mathbf{V} - \frac{\mathrm{d}\mathbf{V}_{cyl}}{\mathrm{d}\tau} = 0 \ . \tag{2.21}$$

A trial solution is substituted into equation 2.21. The RHS of the equation would be zero if the trial solution is the exact solution of the equation. If the trial solution is not the exact solution but an approximation to the exact solution which is the case in general, then the RHS will be non-zero and a residual will be formed. This residual could be defined by,

$$\frac{\partial \mathbf{V}_{trial}}{\partial \tau} + \nabla P_{trial} - \frac{1}{Re}(\nabla^2 \mathbf{V}_{trial}) + (\mathbf{V}_{trial}.\nabla)\mathbf{V}_{trial} - \frac{\mathrm{d}\mathbf{V}_{cyl}}{\mathrm{d}\tau} = \mathbf{R} \ , \tag{2.22}$$

The trial solutions for velocity and pressure fields are $\mathbf{V}_{trial}$ and P_{trial} respectively. The error term which is introduced through the trial function is the residual $\mathbf{R}$. It is clear from equation 2.22 that the definition of the residual is the governing equation substituted by the trial solution substituted to the true solution.

In order to effectively distribute the error over the domain, the residual has to be weighted in order to minimise the maximum local error. To perform this task the inner product of the residual with a series of weighing functions were taken. The integral of the product of the weighting function and the residual is the inner product of the residual which is set to zero. The method employed here is also commonly known as weighted residual method.

Tensor-product Lagrange polynomials were used for both interpolating trial functions and weighting functions in the DNS carried out in this study. The order of the polynomials p could be varied from 2 to 14 in order to further improve grid resolution which is also known as p refinement. This p refinement coupled with h refinement leads to a method called $h-p$ method which is used to improve accuracy (Karniadakis and Sherwin, 2005). The method also could be referred as a Galerkin method as both trial and weighting functions used were from the same family of functions. Fletcher (1984, 1991) provides further details on weighted-residual methods and Galerkin method.

Lagrange polynomials could be defined as,

$$L_i(\xi) = \prod_{\substack{g=1 \\ g \neq i}}^{p+1} \frac{(\xi - \xi_g)}{(\xi_i - \xi_g)} \tag{2.23}$$

The special coordinate is ξ and the indices of the data points are represented by i and g and the number of data points are represented by $p+1$. One of the properties of Lagrange polynomials is that being equal to unity at the point i and being zero at all the other points other than in places in between points. Thus a continuous polynomial which matches the exact values of the velocity at the node point could be obtained when L_i is multiplied by the velocity at point i and then summing over all points. The tensor-product polynomials in two dimensions $N_{q,s}(\xi, \eta)$ could defined as the product of the Lagrange polynomial in one direction $L_q(\xi)$, with that in the other direction $.L_q(\eta)$

The outline of the procedure to find the solution is as follows. The process is initiated by forming inner product of the residual and the tensor-product Lagrange polynomial weighting function.

This gives the integral

$$\int \int_{\Omega} N_{k,m}(\xi,\eta) \cdot [\frac{\partial \mathbf{V}_{trial}}{\partial \tau} + \nabla P_{trial} - \frac{1}{Re}(\nabla^2 \mathbf{V}_{trial}) + (\mathbf{V}_{trial} \cdot \nabla)\mathbf{V}_{trial} - \frac{\mathrm{d}\mathbf{V}_{cyl}}{\mathrm{d}\tau}]\mathrm{d}x\mathrm{d}y = 0 \ ,$$

$$(2.24)$$

The computational domain is represented by Ω. $N_{q,s}(\xi,\eta)$ are the weighting function as defined in the computational space.

From equation 2.24 it is shown that each term in the equation is multiplied by the weighting function. Thus, the integral is split into components and the process could be carried out in the each of the substep equations 2.8, 2.9 and 2.10. For example the discretised equation for 2.13 could be expressed as

$$\frac{1}{\Delta \tau} \int \int_{\Omega} N_{q,s}(\xi,\eta) \cdot (\mathbf{V}_{trial}^* - \mathbf{V}_{trial}^{(n)} - \Delta \mathbf{V}_{cyl})\mathrm{d}x\mathrm{d}y =$$

$$\int \int_{\Omega} N_{q,s}(\xi,\eta) \cdot (\frac{1}{12}(23\mathbf{N}(\mathbf{V}_{trial})^{(n)} - 16\mathbf{N}(\mathbf{V}_{trial})^{(n-1)} + 5\mathbf{N}(\mathbf{V}_{trial})^{(n-2)}))\mathrm{d}x\mathrm{d}y \ . \quad (2.25)$$

This integral could be broken into components. Hence, the first term of the of the LHS of equation 2.25 could be defined as,

$$\int \int_{\Omega} \mathbf{V}_{trial}^* N_{q,s}(\xi,\eta)\mathrm{d}x\mathrm{d}y \ . \quad (2.26)$$

The first term in equation 2.13 could be used as an example to illustrate the process of obtaining the solution using the spectral element method. In order to calculate the integral of equation 2.26 over the entire computational domain, the integral is evaluated over each element separately. After that, the contributions of each element are summed together.

All the quadrilateral elements are mapped to a square ranging between $-1, 1$ in both directions where ξ and η are the orthogonal coordinates of this square. The approximation of the integral is simplified by defining the internal node points with the Gauss-Lobatto-Legendre (GLL) quadrature.

A Jacobian is introduced to perform this coordinate transformation and hence, the integral over each element becomes,

$$\int \int_{El} \mathbf{V}^* N_{q,s}(\xi,\eta)\mathbf{J}(\xi,\eta)\mathrm{d}\xi\mathrm{d}\eta \ , \quad (2.27)$$

The Jacobian represented by $\mathbf{J}$ and "El" denotes that the integration is performed over a single element. The solution of equation 2.27 $\mathbf{V}_{trial}^*$, could be re-written as a summation

of Lagrange polynomial components. This equation also expresses the tensor-product Lagrange polynomials representing the weighting functions in directions of ξ and η. Therefore, the equation could be expressed as,

$$\int \int_{El} \sum_{i,j} \widehat{\mathbf{V}^*} L_i(\xi) L_j(\eta) L_q(\xi) L_s(\eta) \mathbf{J}(\xi,\eta) \mathrm{d}\xi \mathrm{d}\eta \ . \tag{2.28}$$

The velocity in the nodal points are represented by $\widehat{\mathbf{V}^*}$, L is the one-dimensional Lagrange polynomial and i and j represents the node index in directions ξ and η.

The Gauss-Lobatto Legendre (GLL) quadrature could be used to obtain an approximation to the integral in equation 2.28, taking the definition of the location of the internal points in the computational domain. Thus approximation of 2.28 could be expressed as,

$$\sum_{a,b} W_{a,b} \sum_{i,j} \widehat{\mathbf{V}^*}_{i,j} L_i(\xi_a) L_j(\eta_b) L_q(\xi_a) L_s(\eta_b) \mathbf{J}(\xi_a,\eta_b) \ . \tag{2.29}$$

$W_{a,b}$ represents the weighting coefficient for GLL quadrature, a and b represents the position of the node in the directions ξ and η respectively.

Even though equation 2.29 appears to be quite intimidating to deal with, the expression could be considerably simplified because of the fact that the system is discrete and the only values at the nodal points are considered. Incorporating Lagrange polynomials allows the substitution

$$Ł_i(\xi_a) = \delta_{ia} = \begin{cases} 1 & i = a \\ 0 & i \neq a \end{cases} \ . \tag{2.30}$$

The Kronecker delta is expressed by δ_{ia}. This substitution leads to a significant reduction of the non-zero elements in the simulation and leads to a much simpler expression. If the convection substep (example considered here) is considered, only a single term remains based on the $\mathbf{V}^*$ term in the convection substep equation which is,

$$W_{q,s} \mathbf{J}(\xi_q,\eta_s) \widehat{\mathbf{V}^*}_{q,s} \ . \tag{2.31}$$

All the governing terms could be simplified similarly and this process is repeated over all elements. A global matrix is assembled by collecting the contribution of each element

and then this matrix system is solved to obtain solution for the unknown velocity and pressure fields at the nodal points.

Only the continuity of each function is required across the boundaries, with no condition imposed on the gradient (this condition is known as C_0 continuity), even though the shape functions are higher-order polynomials within each element. It can be shown that the method achieves global exponential convergence (Karniadakis and Sherwin, 2005).

The numerical process used for this study has been demonstrated to give exponential spatial convergence as the number of internal nodes per element is increased (Thompson et al., 1996).

Boundary conditions

The boundary conditions, regardless of the mesh were common for all the simulations performed. A no-slip condition was applied to the cross section wall. This condition ensures that the velocity is zero at the surface of the cross section. For stationary simulations a Dirichlet boundary condition is applied. For FSI cases a time-dependent Dirichlet boundary condition was employed for the velocity on the inlet and lateral boundaries. A Dirichlet boundary condition should have a specified value for the variables (Kreyszig, 2010) in this case velocity. The time-dependent Dirichlet condition has to be implemented for the FSI cases to account for the accelerated reference frame attached to the cross section. Thus, the inlet boundary was set to $u = U$ and $v = -\dot{y}$ for FSI cases and $v = 0$ for stationary cases, where u, v are the velocities in the x and y directions, respectively.

The outlet which is at the boundary downstream of the body was assigned the Neumann boundary condition (where the gradient of a property is specified Tu et al. (2008)), $\frac{\partial \mathbf{V}}{\partial \mathbf{n}} = 0$ where $\mathbf{n}$ denotes the unit normal vector. This assumes that the flow does not spatially evolve while exiting the domain.

A Neumann condition for the pressure was applied at all the boundaries except the outlet. The normal gradient was calculated from the Navier–Stokes equations. A Dirichlet condition for the pressure ($p = 0$ was enforced at the outlet. The details of the method can be found in Thompson et al. (2006, 1996)

Although the physical validity of the outlet boundary condition is not quite true, this does not turn out to be a significant problem provided that the Reynolds numbers are low

and the domain is sufficiently far away from the body.

2.4.3 Convergence and validation studies

Domain size

For all cases, a rectangular domain was employed where the inlet was placed $20D$ from the centre of the body, while the outlet was situated $60D$ away from the centre of the body. The lateral boundaries were placed $20D$ away from the centre of the body. The macro element arrangement of the general domain is shown figure 2.1. The macro element arrangement near the cross section was altered to cater for different cross sections. The near wall macro element configuration for the different cross sections are presented in figure 2.2.
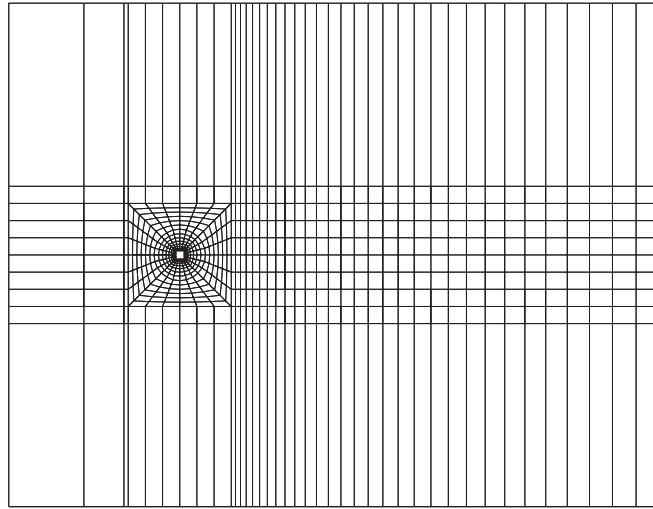
Figure 2.1: Macro element arrangement in the domain for the square cross section geometry. The inlet extending $20D$ upstream from the centre of the body, while the outlet extends $60D$ downstream from the centre of the body. The lateral boundaries were placed $20D$ away from the centre of the body

Convergence

A series of simulations were carried out in order to ensure the results were grid independent. This was done by by keeping the layout of the macro element the same and varying the

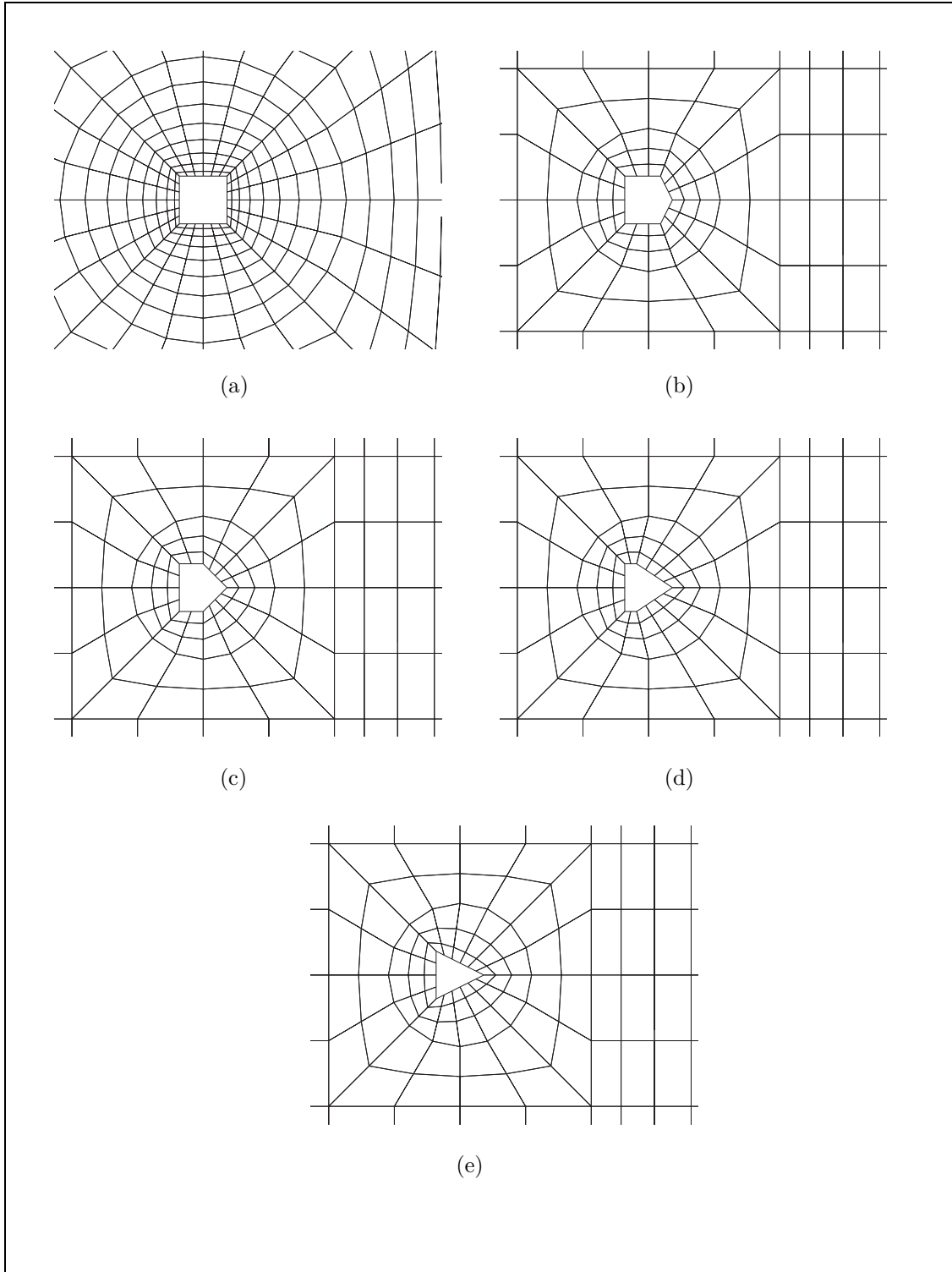Figure 2.2: Configuration of the macro elements near the cross section. (a) square, (b) $\frac{d}{l} = 0.75$, (c) $\frac{d}{l} = 0.5$, (d) $\frac{d}{l} = 0.25$ and (e) triangle.
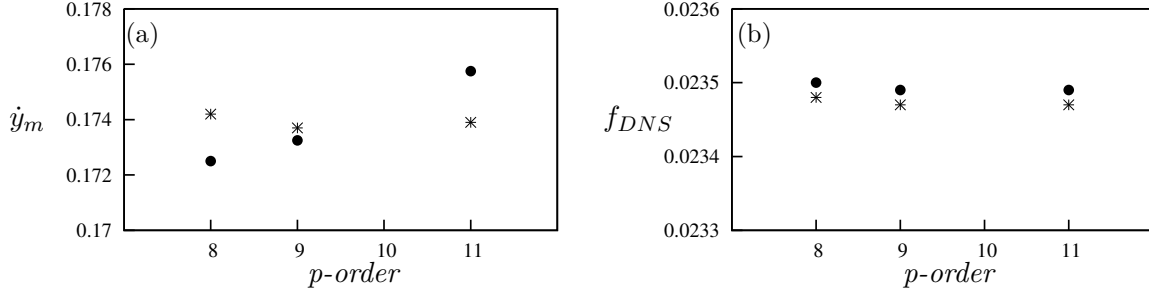
Figure 2.3: Mean velocity amplitude ($\dot{y}_m$) (a) and the galloping frequency (f_{DNs}) (b) as a function of the interpolation polynomial. Data present $\frac{tU}{D} = 0.001$ (✳) and $\frac{tU}{D} = 0.0005$ (•). Data acquired $Re = 200$ $\Pi_2 = 0$ using FSI direct numerical simulations.

order of the interpolation polynomial (*p-refinement*). The displacement amplitudes were compared against various polynomial orders. The time step is also reduced as the special resolution increases to satisfy the Courant condition. The summary of the results are presented in figure 2.3 .

Figure 2.3 shows the mean velocity amplitude (sub-figure (a)) and the galloping frequency (sub-figure (b)) at different polynomial orders. Two factors namely, the quantitative accuracy of the data and the computational time had to be considered during the decision making process to obtain the optimum spacial and temporal resolution. Even though higher order polynomials gave very accurate data, the time step has to be reduced accordingly to meet the Courant condition and therefore increasing computational time. Thus a 9th order polynomial was incorporated with $\frac{tU}{D} = 0.001$ time-step. A difference of less than 1% could be achieved for both mean velocity amplitude of the body and galloping frequency using this spatial and temporal parameters.

The FSI simulations for other cross sections presented in this thesis were also carried out using these special and temporal parameters.

CHAPTER 3

INTRODUCTION

The review of published literature reveals that fluid-elastic galloping has a potential to be used as a mechanism for energy extraction (Barrero-Gil et al., 2010). Thus, the following questions emerged. What are the optimum parameters for energy transfer in a galloping system? How do they influence galloping?

Another fluid-structure interaction phenomenon, vortex-induced vibration (VIV), has also been investigated as a candidate for the power extraction from flows. The work from Bernitsas et al. (2008, 2009); Raghavan and Bernitsas (2011); Lee and Bernitsas (2011) and others from the same group at the University of Michigan have made significant progress with this problem. Therefore it may seem, at least initially, reasonable to present data from the fluid-elastic problem in the same parameters as typically used in VIV studies, which could be observed in current literature on galloping (Barrero-Gil et al., 2009, 2010; Parkinson and Smith, 1964).

However, the data presented in the pioneering study on energy harvesting from galloping (Barrero-Gil et al., 2010) presented using classical VIV parameters (i.e. U^*, $m^*\zeta$), shows that the mean power data does not collapse well. The reason behind for this hypothesis to be the difference in time-scales of VIV and galloping. Thus the work presented in this chapter is focused on testing this hypothesis and obtain the optimum conditions for mean power output.

Since the the Quasi-steady state model is the primary mathematical model used to model galloping in this study, the fluid-dynamic characteristics of flow over a static body

are presented and discussed first as it is the main input to the QSS model. Then, the natural time scales of the system are obtained using the linearised QSS model. Next, the new non-dimensional governing parameters Π_1 and Π_2, are formulated by non-dimensionalising the QSS model from these natural time scales. Following this a comparison of galloping data using the classical VIV parameters and Π_1 and Π_2. Then, the influence of Π_1 and Π_2 and the conditions for an optimum power output are discussed from QSS data. Finally, the QSS data are compared and discussed against FSI direct numerical simulations and final conclusions are presented.
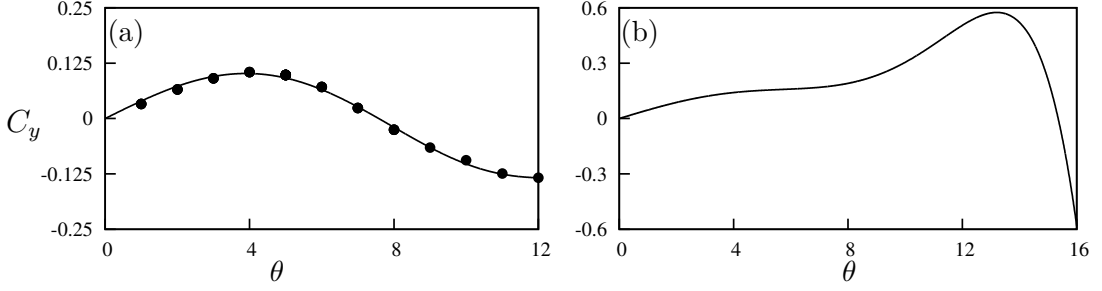
Figure 3.1: Lift coefficient, C_y, as a function of incidence angle θ, for a static square cross section. (a) Data from simulations at $Re = 200$ and (b) data from Parkinson and Smith (1964) at $Re = 22300$. The values at points ($\bullet$) are acquired from direct numerical simulations . Curves in both plots are 7th-order interpolating polynomials used to interpolate the fluid forcing for the QSS model.

3.0.1 Static body results

The main data acquisition tool for galloping is the QSS model. As discussed in chapter 2.2,the input to the QSS model is the lift force as a function of the induced angle of attack θ. This function is obtained using lift and drag (C_y) data from static body simulations or experiments, to which a polynomial is fitted. These static body data and the polynomial data are presented here in 3.1 and 3.1 respectively. Figure 3.1 shows the plots of time averaged C_y data as a function of θ, as well as the 7th order polynomial fits . Data are acquired for high and low Reynolds numbers. For high Reynolds numbers, the static body polynomial data are obtained from Parkinson and Smith (1964) while for low Reynolds numbers a 7th order non-linear least square regression fit on static body DNS simulations was used. The coefficients of these polynomials are presented in table 3.1.

There are several differences that can be observed between high and low Reynolds number data. The peak value of C_y is significantly lower at $Re = 200$ ($C_y = 0.12$ at $5°$) compared to $Re = 22300$ ($C_y = 0.57$ at $13°$) . The inflection point present around $8°$ for $Re = 22300$ is not present at $Re = 200$. This agrees with the findings of Luo et al. (2003). Luo et al. (2003) concluded that hysteresis in the system response occurs due to the inflection point in the C_y curve. Therefore, hysteresis could not be observed at $Re = 200$.

The range of incident flow angles where C_y remains positive is narrow at $Re = 200$ ($0° < \theta \leq 7°$) compared to $Re = 22300$ ($0° < \theta \leq 15°$). This positive range sustains

Case	a_1	a_3	a_5	a_7
$Re = 200$	2.32	197.8	4301.7	30311.9
$Re = 22300$	2.69	168	1670	59900

Table 3.1: Coefficient values used in the 7th order interpolation polynomial for high ($Re = 22300$) and low ($Re = 200$) Reynolds numbers. These data are used as input data to calculate the right-hand side of Eq. 1.4 throughout this study.

galloping, as the power is only transferred from the fluid to the supporting structure within this range of incident angles. This is because the fluid forces are acting in the direction of velocity of the body, or in phase with, the oscillating body as demonstrated by equation 2.2. Incident angles beyond this range suppress the galloping as power is transferred in the opposite direction, i.e; from body to fluid. Thus, it is expected that the transferred power at $Re = 200$ to be significantly lower than at $Re = 22300$, because of the relatively low values of C_y and the narrow range of positive C_y at $Re = 200$.

3.0.2 Formulation of the new dimensionless groups suitable to obtain optimum power output Π_1 and Π_2

The natural time scales of the system can be found by solving for the eigenvalues of the linearised equation of motion (Eq:1.4), namely

$$m\ddot{y} + c\dot{y} + ky = \frac{1}{2}\rho U^2 \mathcal{A} a_1 \left(\frac{\dot{y}}{U} \right), \tag{3.1}$$

which is a simplified version of the equation of motion presented in equation 1.4 with the polynomial series for the lift force truncated at the linear term.

Combining the $\dot{y}$ terms and solving for eigenvalues gives

$$\lambda_{1,2} = -\frac{1}{2}\frac{c - \frac{1}{2}\rho U \mathcal{A} a_1}{m} \pm \frac{1}{2}\sqrt{\left[\frac{c - \frac{1}{2}\rho U \mathcal{A} a_1}{m} \right]^2 - 4\frac{k}{m}}. \tag{3.2}$$

If it is assumed that the spring is relatively weak, $k \to 0$, a single non-zero eigenvalue

remains. This eigenvalue is

$$\lambda = -\frac{c - \frac{1}{2}\rho U \mathcal{A} a_1}{m}. \tag{3.3}$$

Further, if it is assumed that the mechanical damping is significantly weaker than the fluid-dynamic forces on the body, $c \to 0$ and

$$\lambda = \frac{\frac{1}{2}\rho U \mathcal{A} a_1}{m}. \tag{3.4}$$

In this form, λ represents the inverse time scale of the motion of the body due to the effect of the long-time fluid-dynamic forces. In fact, the terms can be regrouped and λ written as

$$\lambda = \frac{a_1}{m^*}\frac{U}{D} \tag{3.5}$$

Written this way, the important parameters that dictate this inverse time scale are clear. The rate of change in the fluid-dynamic force with respect to angle of attack when the body is at the equilibrium position, $\partial C_y/\partial \theta$, is represented by a_1. The mass ratio is represented by m^*. The inverse advective time scale of the incoming flow is represented by the ratio U/D. Increasing a_1 would mean the force on the body would increase more rapidly with small changes in the angle of attack, θ, or transverse velocity. Equation 3.5 shows that such a change will increase the inverse time scale, or analogously decrease the response time of the body. Increasing the mass of the body, thereby increasing m^*, has the opposite effect. The inverse time scale is decreased, or as might be expected, a heavier body will respond more slowly.

This timescale can then be used to non-dimensionalize the equation of motion, and to find the relevant dimensionless groups of the problem. It was suggested by Shiels et al. (2001); Leonard and Roshko (2001) to use a flow-based timescale such D/U for the characteristic time for flow-induced vibration problems, rather than a structural-based timescale such as the natural frequency. This point is discussed further in Williamson and Govardhan (2004). Here, this advective time is further scaled by the mass ratio m^*, as suggested from the eigenvalues of the linearized equation of motion. Hence, if the non-dimensional time, τ, is defined such that $\tau = t(a_1/m^*)(U/D)$, the equation of motion presented in equation 1.4 can be non-dimensionalized as

$$\ddot{Y} + \frac{m^{*2}}{a_1^2}\frac{kD^2}{mU^2}Y = \left(\frac{1}{2} - \frac{m^*}{a_1}\frac{cD}{mU}\right)\dot{Y} - \frac{a_1 a_3}{m^{*2}}\dot{Y}^3 + \frac{a_1^3 a_5}{m^{*4}}\dot{Y}^5 - \frac{a_1^5 a_7}{m^{*6}}\dot{Y}^7. \tag{3.6}$$

The coefficients can be regrouped into combinations of non-dimensional groups, and rewritten as

$$\ddot{Y} + \frac{4\pi^2 m^{*2}}{U^{*2} a_1^2} Y = \left(\frac{1}{2} - \frac{c^* m^*}{a_1} \right) \dot{Y} - \frac{a_1 a_3}{m^{*2}} \dot{Y}^3 + \frac{a_1^3 a_5}{m^{*4}} \dot{Y}^5 - \frac{a_1^5 a_7}{m^{*6}} \dot{Y}^7, \qquad (3.7)$$

where U^* is the reduced velocity typically used as an independent variable in vortex-induced vibration studies and $c^* = cD/mU$ is a non-dimensional damping parameter.

Equation 3.7 shows there are five non-dimensional parameters that play a role in setting the response of the system. These are the stiffness (represented by the reduced velocity U^*), the damping c^*, the mass ratio m^*, and the geometry and Re, represented by the coefficients of the polynomial fit to the C_y curve, a_n. The grouping of these parameters into two groups in equation 3.7 which arise by non-dimensionalising using the natural time scale of the galloping system, suggests there are two groups besides geometry (represented by a_n) and Re that dictate the response: $\Gamma_1 = 4\pi^2 m^{*2}/U^{*2} a_1^2$ and $\Gamma_2 = c^* m^*/a_1$. For a given geometry and Reynolds number, Γ_1 can be thought of as a combined mass-stiffness, whereas Γ_2 can be thought of a combined mass-damping parameter. It is assumed that during galloping the stiffness plays only a minor role because galloping time periods are significantly large which implies that $k \rightarrow 0$. Therefore, Γ_2 seems a likely parameter to collapse the data. In fact, in the classic paper on galloping from Parkinson and Smith (1964), galloping data from wind tunnel tests is presented in terms of a parameter that can be shown to be the same as Γ_2.

All of the quantities that make up Γ_1 and Γ_2 can, in theory, be known before an experiment is conducted. However, the quantity a_1 is a relatively difficult one to determine, requiring static body experiments or simulations. Here, the geometry is unchanged and results are only being compared at the same Re. Hence, suitable parameters can be formed by multiplying Γ_1 and Γ_2 by a_1^2 and a_1 respectively, to arrive at a mass-stiffness parameter $\Pi_1 = 4\pi^2 m^{*2}/U^{*2}$, and a mass-damping parameter defined as $\Pi_2 = c^* m^*$.

Equation 3.7 can be re-written explicitly in terms of Π_1 and Π_2 to give

$$\ddot{Y} + \Pi_1 Y = \Pi_2 \dot{Y} - \frac{a_1 a_3}{m^{*2}} \dot{Y}^3 + \frac{a_1^3 a_5}{m^{*4}} \dot{Y}^5 - \frac{a_1^5 a_7}{m^{*6}} \dot{Y}^7. \qquad (3.8)$$

3.0.3 Comparison of Π_1 and Π_2 with classical VIV parameters

Figure 3.2 shows the comparison of mean power data at $Re = 200$ presented using different independent variables. Subfigures (a), (c) and (e) show the displacement amplitude, velocity amplitude and the mean power as a function of the classic VIV parameter, U^* for various damping ratios ζ. Subfigures (b), (d) and (f) shows the same data as a function of Π_2, for various, reasonably high values of Π_1, as defined above in section 3.0.2. The data presented using the classical VIV parameters follows the same trends as Barrero-Gil et al. (2010). Barrero-Gil et al. (2010) and Vicente-Ludlam et al. (2014) observed that the maximum dimensionless power is achieved at two times the velocity at which the galloping starts. A similar conclusion can be drawn from the data presented here in figures 3.2. However, the data presented using the dimensionless group formulated using the natural time scales of the system shows an excellent collapse for both velocity amplitude and mean power, showing that the power is essentially dictated by Π_2. This implies that unlike VIV which is a type of resonant phenomenon, the natural frequency of the system which is used to scale U^*, ζ and Π_1 does not have a large influence on the system behaviour in these cases.

Figure 3.2 shows the displacement]amplitude data obtained in figure 3.2 (a)

3.0.4 Comparison of power between high and low Re data

The marked success of the collapse using Π_2 for the $Re = 200$ case, particularly of the mean power, could also be replicated for the higher Re case at $Re = 22300$. Figure 3.4 presents the mean power for high Re cases for selected values of Π_1. It is shown that the data collapse in both cases, demonstrating the validity of using Π_2 as an independent variable.

Hysteresis could be observed for the $Re = 22300$ case. The different solutions could be obtained by manipulating the initial conditions (initial displacement) of the system. The upper branch was obtained by giving an initial displacement which was higher than the expected amplitude while the lower branch was obtained by providing a lower initial displacement than the expected amplitude. Although theory shows a possible third state, it is an unstable branch which could not be achieved with a time integration method such as that employed in this study. This was also observed by Vio et al. (2007).
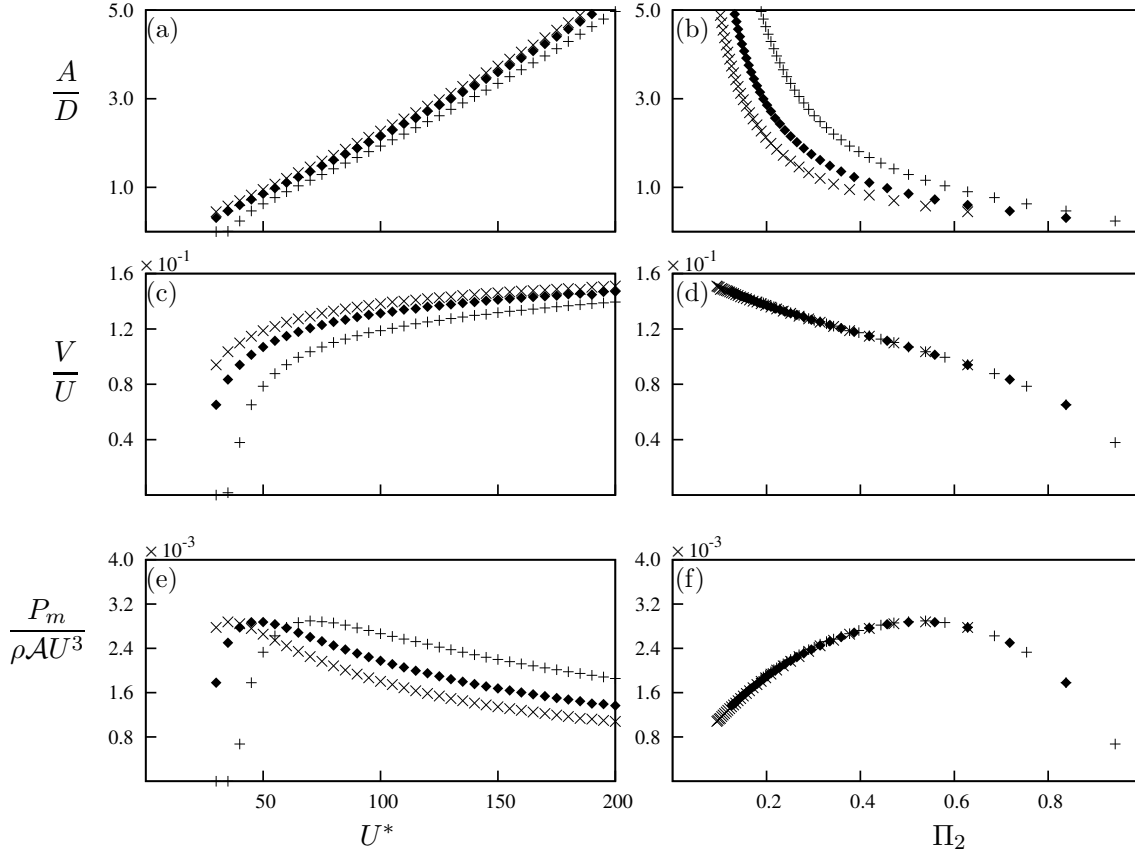
Figure 3.2: Displacement amplitude, velocity amplitude and dimensionless mean power data as functions of two different independent variables. Data presented in (a), (c) and (e) using the classical VIV parameter U^*, obtained at $Re = 200$ and $m^* = 20$ at three different damping ratios: $\zeta = 0.075$ ($\times$), $\zeta = 0.1$ ($\blacklozenge$) and $\zeta = 0.15$ ($+$). (b) (d) and (f) are the same data presented using the combined mass-damping parameter (Π_2) as the independent variable. Even though Π_1 varies in the range of $0.4 \leq \Pi_1 \leq 17.5$, it is clear that the power is a function of Π_2 only.
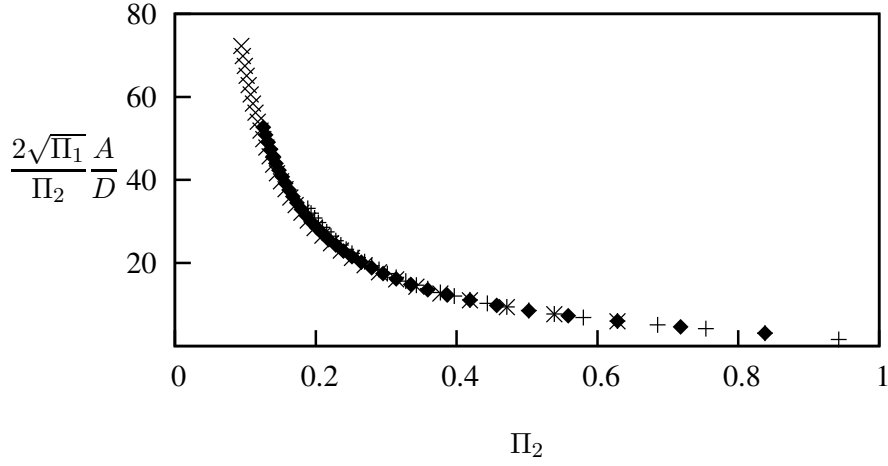
Figure 3.3: Displacement amplitude data as function of Π_2. obtained at $Re = 200$ and $m^* = 20$ at three different damping ratios: $\zeta = 0.075$ ($\times$), $\zeta = 0.1$ ($\blacklozenge$) and $\zeta = 0.15$ (+). Both the dependent variable is scaled with $\frac{2\sqrt{\Pi_1}}{\Pi_2}$ which is equal to $\frac{1}{\zeta}$. This scaling is similar to Parkinson and Smith (1964) and the deviation of data using this scaling at high U^* could be observed in Parkinson and Smith (1964)
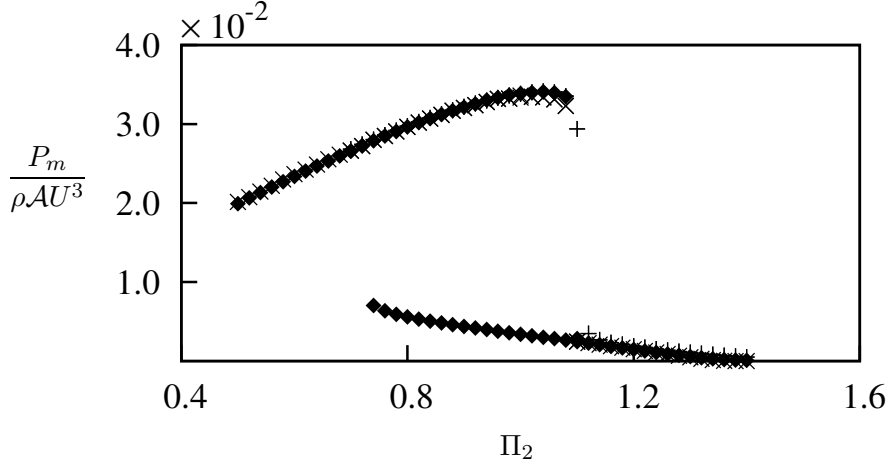
Figure 3.4: Dimensionless mean power as a function of Π_2. Data presented at $Re = 22300$, $\Pi_1 = 200$ ($\times$), $\Pi_1 = 2000$ ($\blacklozenge$) and $\Pi_1 = 10000$ (+). Hysteresis could be observed at high Re.

3.0.5 Dependence on mass-stiffness, Π_1

The results of sections 3.0.3 and 3.0.4 show that the mean extracted power is essentially a function of a single variable, the combined mass-damping Π_2. However, the timescale analysis of section 3.0.2 showed that a second variable, the combined mass-stiffness Π_1 should also play a role. Previous studies (see, for example Bouclin (1977)) have also indicated a complex interaction between the amplitude and natural frequency, particularly for high natural frequencies (or equivalently, low values of Π_1). Here, the impact of Π_1 is investigated further. Overall, the system behaviour can be separated into two wide regimes; that for "high" Π_1 and that for "low" Π_1. These two regimes are further investigated and explained in this following section.

Figure 3.5 shows the mean power as a function of Π_2 for a range of values of Π_1. Two subfigures are shown; subfigure (a) shows data for $\Pi_1 \geq 10$, while (b) shows data for $\Pi_1 \leq 10$. In figure 3.5(a), the collapse of the mean power is excellent, showing that for $\Pi_1 \geq 10$, the mean power is independent of Π_1.

For low values of $\Pi_1 \leq 10$, figure 3.5(b) shows that the predicted mean power increases as Π_1 is decreased, indicating that the mean power is a weak function of Π_1 at low Π_1 levels. This provides the distinction between high and low Π_1 regimes. For high values where $\Pi_1 \geq 10$, the mean extracted power is a function of Π_2 only; for low values where
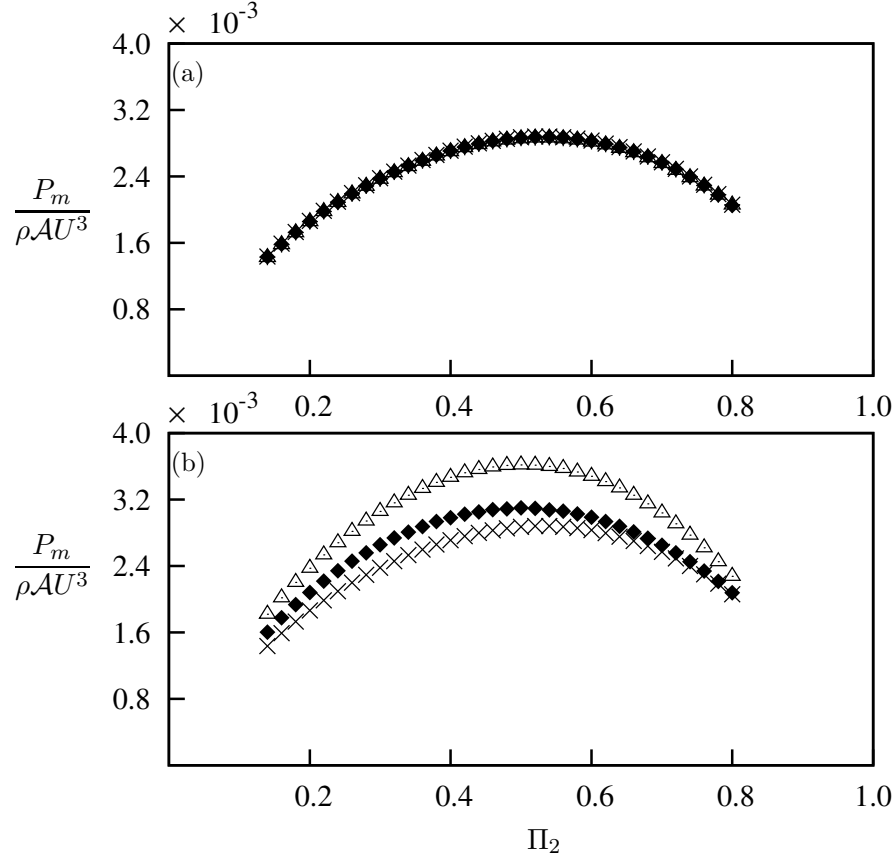
Figure 3.5: Dimensionless mean power as a function of Π_2 obtained using the QSS model at $Re = 200$. (a) High Π_1; data presented at four different combined mass-stiffness levels. $\Pi_1 = 10$ ($m^* = 20$, $U^* = 40$) ($\times$), $\Pi_1 = 100$ ($m^* = 80$, $U^* = 50$) (+), $\Pi_1 = 500$ ($m^* = 220$, $U^* = 60$) ($\blacklozenge$) and $\Pi_1 = 1000$ ($m^* = 400$, $U^* = 40$) ($\triangle$). (b) Low Π_1; data presented at $\Pi_1 = 10$ ($\times$), $\Pi_1 = 0.1$ ($\blacklozenge$), and $\Pi_1 = 0.01$ ($\triangle$).

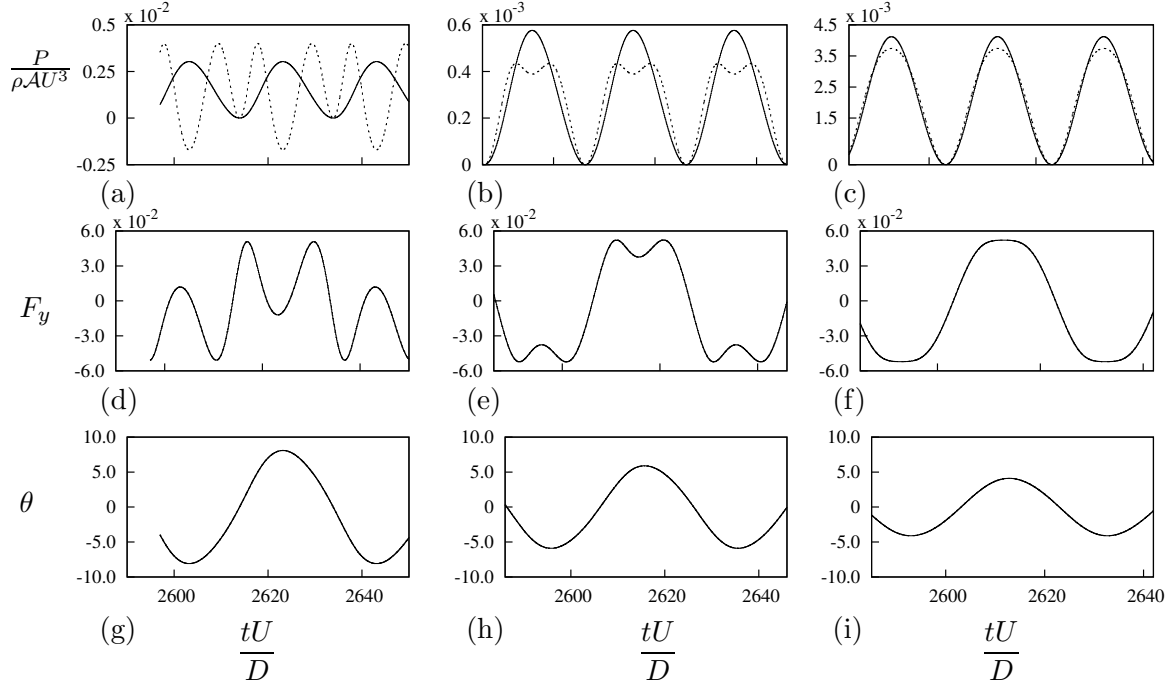Figure 3.6: Time histories of P_t, P_d, F_y and θ at $\Pi_2 = 0.15$, 0.54 and 0.8 from the QSS model. Data was obtained at $m^* = 20$, $\Pi_1 = 10$ and $Re=200$. The time histories of P_d (—) and P_t (- - -) are presented for: (a) $\Pi_2 = 0.15$; (b) $\Pi_2 = 0.54$; (c) $\Pi_2 = 0.8$. Time histories of the instantaneous force F_y for: (d) $\Pi_2 = 0.15$; (e) $\Pi_2 = 0.54$; (f) $\Pi_2 = 0.8$. Time histories of the instantaneous angle θ for: (g) $\Pi_2 = 0.15$; (h) $\Pi_2 = 0.55$; (i) $\Pi_2 = 0.8$.

$\Pi_1 < 10$, the mean extracted power is a weak function of Π_1.

Regardless of the value of Π_1, the variation of the mean extracted power with Π_2 is essentially the same. With increasing Π_2, the mean extracted power initially increases, before reaching some maximum value and then decreasing. This relationship between power and Π_2 can be explained by analysing the time histories of selected cases. Data at $\Pi_1 = 10$, $m^* = 20$ and $Re = 200$ are shown in figure 3.6 and are analysed as an example. Values of Π_2 less than (region 1), equal to (region 2), and greater than (region 3) the value where the mean extracted power is a maximum are analysed as examples.

The instantaneous power from the fluid to the body can be expressed as $P_t = F_y \dot{y}$. Similarly the dissipated power due to the mechanical damping can be expressed as $P_d = (c\dot{y})\dot{y}$. The time average of these two quantities, described in equations 2.1 and 2.2 must be equal due to energy conservation.

At region 1 ($\Pi_2 = 0.15$) the damping is low in comparison with region 2 and 3. While this may lead to larger oscillations, damping is required to dissipate and therefore extract power according to equation 2.1. Therefore, the low damping in this region leads to a low mean power output. Fig.3.6 (a) shows that P_d (the power dissipated by damping) becomes negative over some portion of the cycle. This is caused by the high velocity amplitude leading to the equivalent incident angle θ to exceed the range where C_y is positive (i.e. $0 < \theta < 6°$ as shown in figure 3.1(a)). In this portion of the cycle the fluid-dynamic force actually opposes the direction of travel and power is transferred from the structure to the fluid during those times. From an energy perspective, the mechanical damping is not sufficient to remove the energy transferred from the fluid to the structure through work during other times of the cycle because Π_2 is substantially low. Therefore this excess energy is transferred back to the fluid as depicted by the negative region of P_d.

At region 3 where $\Pi_2 = 0.8$ the damping constant is high and a clear sinusoidal signal is observed for both P_d and P_t in figure 3.6(c). Figures 3.6(f) and 3.6(i) show that equivalent incident angle θ (which for small values, is proportional to the transverse velocity of the body) is in phase with F_y. The velocity amplitude in this case is small and θ is within the range where the fluid-dynamic force increases with the incident angle (i.e. $0 < \theta \leq 5°$ as shown in figure 3.1(a)). According to equation 2.2, these conditions are suitable for high power output. However in this case, the high damping limits the velocity amplitude and results in relatively low fluid dynamic forces.

At region 2 ($\Pi_2 = 0.54$), a balance is found between high and low values of damping. P_d is not a pure sinusoidal signal, however the signal remains periodic. From the time history graph of P_d, two 'peaks' are present in a single half cycle as shown in figure 3.6(b). In this case, the velocity amplitude actually exceeds the equivalent incident angle where the fluid-dynamic forces peaks (i.e. $\theta = 5°$ in figure 3.1 (a)). The dips in P_d between the two peaks approximately correspond to the time where the transverse velocity is higher than 0.09 (i.e. $\theta = 5.14$) and F_y is decreasing with increasing transverse velocity. The mean power output is at its maximum. This is due to the fact that this region is the best compromise between region 1 and 3. The damping is high enough to obtain a high power output while not so high that the motion is completely suppressed.
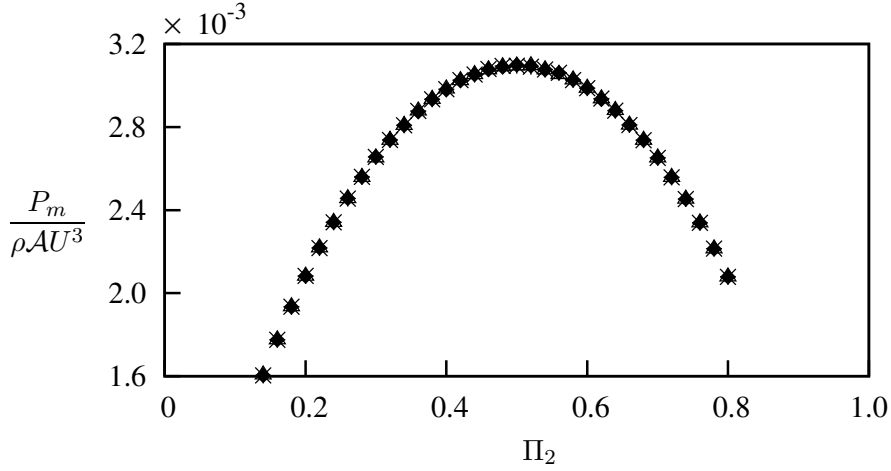
Figure 3.7: Dimensionless mean power as a function of Π_2 obtained using QSS model at $\Pi_1 = 0.1$. Data presented at $m^* = 2$ ($\blacklozenge$), $m^* = 20$ ($\triangle$) and $m^* = 50$ ($*$). The mass ratio does not have an effect on Π_1 even at low Π_1.

3.0.6 Dependence on the mass ratio m^*

While for high values of Π_1 it is clear that the mean extracted power is a function of Π_2 only, a question arises for low values of Π_1; is the variation in the mean extracted power purely a function of Π_1, or is it also a function of the mass ratio m^*? To answer this question, the model has been solved for a fixed value of Π_1, but for varying values of m^*. This means that Π_1 was varied by changing the system stiffness.

Figure 3.7 shows the mean extracted power as a function of Π_2, for a fixed $\Pi_1 = 0.1$, for three different values of m^*. From the figure it is clear that the results are independent of m^*, and are a function of Π_1 and Π_2 only.

3.0.7 Comparison with DNS data

The QSS model assumes that the only force driving the system is the instantaneous lift, which is same as the mean lift on a static body at the same angle of attack. However, vortex shedding is also present in this system. Therefore, an essential assumption when this model is used, is that the effect of vortex shedding is minimal. Hence, the model has been always used at high Re and at high mass ratios because at those Reynolds numbers and mass ratios, the vortex shedding does not correlate across the span. This study is focused on identifying the limiting parameters of the QSS model at low Reynolds numbers

by providing a comparison with DNS results.

Joly et al. (2012) showed that the displacement data obtained using the QSS assumption and DNS agree well at low Reynolds numbers, with the modification implemented to the oscillator equation which accounts for the vortex shedding. These data were obtained at zero damping levels. However, the current study is focused on the behaviour and the power transfer of the system. Therefore analysing the behaviour of the system with increasing damping is of interest.

The comparison between QSS and the DNS results is presented in figure 3.8. The maximum displacement, velocity and mean extracted power are presented as a function of Π_2. A range of values of Π_1 are compared to the QSS model data for $\Pi_1 = 10$. Figures 3.8(a) and 3.8(b) show little variation with Π_1, and the comparison between the QSS model and the DNS simulations is quite good. However, the mean extracted power shown in figure 3.8(c) reveals that the mean power is influenced by both Π_1 and Π_2. This is particularly clear for low values of Π_1, where the discrepancy between the QSS model predictions of power and the DNS simulations is the largest. Comparing figure 3.8(c) with figure 3.5(a) shows that Π_1 has much more influence on the power extracted than predicted by the QSS model for low Π_1 values. In fact, the QSS model predicts that the mean extracted power should increase with decreasing Π_1 when Π_1 moves to the low Π_1 region (figure 3.5(b)), whereas the DNS simulations show that the mean extracted power decreases with decreasing Π_1.

Figure 3.9(a) clearly shows the dependence of the mean extracted power on Π_1. Here, the maximum power extracted for a given value of Π_1, over all values of Π_2(essentially the value of extracted power at the turning point), is plotted as a function of Π_1. These values were obtained by fitting a quadratic to the data of figure 3.7 and finding the value of mean extracted power at the turning point. The rapid decrease in the extracted power as $\Pi_1 \to 0$ is clear.

Figure 3.9(a) also shows that Π_1 is important to higher values than predicted by the QSS model. For the QSS model, the mean extracted power was essentially independent of Π_1 for $\Pi_1 > 10$, as shown by the open symbols on the figure. However, the mean extracted power from the DNS data shows a significant dependence on Π_1 for $\Pi_1 < 250$. Even so, the power extracted during the DNS simulations converges to the value predicted by the

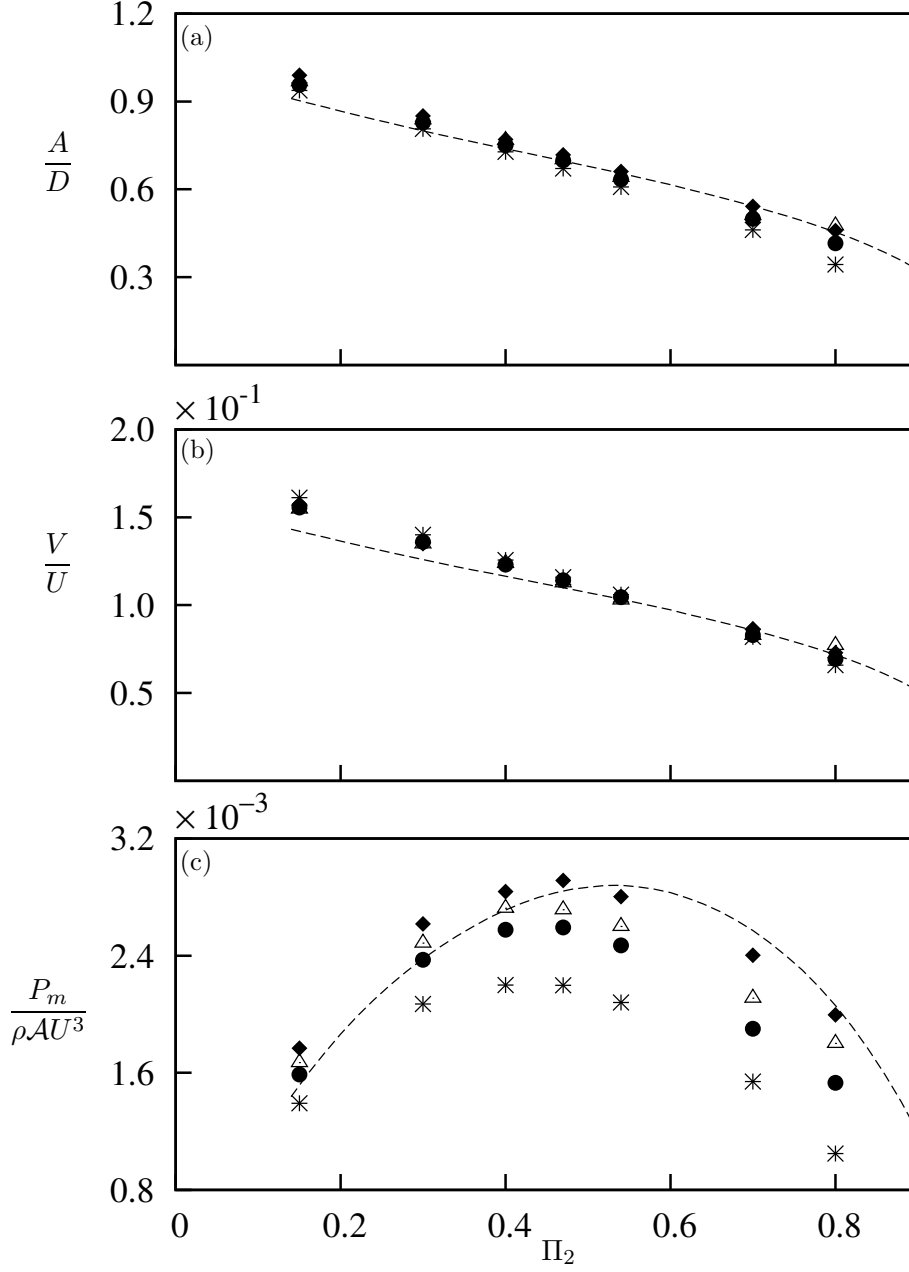Figure 3.8: Comparison of data generated using the quasi-static model and full DNS simulations at (a) Displacement amplitude, (b) velocity amplitude and (c) dimensionless mean power as functions of Π_2. Data were obtained at $Re = 200$ at four values $\Pi_1 = 10$ ($m^* = 20.13$) (✳), $\Pi_1 = 60$ ($m^* = 49.31$) (●), $\Pi_1 = 250$ ($m^* = 100.7$) (△) and $\Pi_1 = 1000$ ($m^* = 201.3$) (◆). The QSS data at $\Pi_1 = 10$ (---).
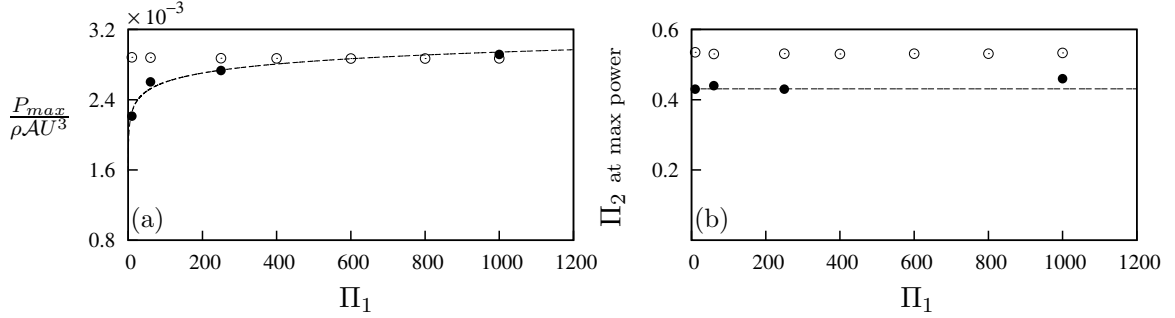
Figure 3.9: (a) Maximum power and (b) the value of Π_2 at maximum power of QSS data ($\circ$) and DNS data ($\bullet$), as functions of Π_1. For the DNS data, the maximum power asymptotes to an upper value with increasing Π_1, while the value of Π_2 where maximum power occurs is relatively insensitive to Π_1. The maximum power of the QSS data remains relatively constant, as does the value of Π_2 where maximum power occurs. The dash curve (---) of (a) follows the logarithmic fit of the maximum power which is $P_{max}/\rho\mathcal{A}U^3 = 1.48 \times 10^{-4} \, log(\Pi_1) + 1.9 \times 10^{-3}$. The dashed curve in (b) shows the value $\Pi_2 \simeq 0.43$.

QSS model as Π_1 increases.

Figure 3.9(b) shows the value of Π_2 at which the turning point, and therefore the maximum power output, occurs. The open symbols show the value predicted by the QSS model, the closed symbols show the value predicted by the DNS. The two are not the same, with a value around 0.41 predicted by the DNS (shown with a dashed line) and a value above 0.5 predicted by the QSS model. However, both models show that while the power extracted is a reasonably strong function of Π_1, the value of Π_2 at which this maximum power occurs is relatively unaffected.

In an effort to further quantify the performance of the QSS model, the percentage between the QSS and DNS extracted power data as a function of Π_1 was calculated using the equation

$$\% \, error = \left| \frac{P_{m(QSS)} - P_{m(DNS)}}{P_{m(DNS)}} \right| \times 100. \tag{3.9}$$

The results of this calculation are plotted in figure 3.10, along with a power-law best fit $138.697\Pi_1^{-0.6}$. The figure clearly shows that as Π_1 increases, the error between the QSS and DNS models quickly decreases. However, at low values of Π_1, the discrepancy between the two can be quite large, around 30%.
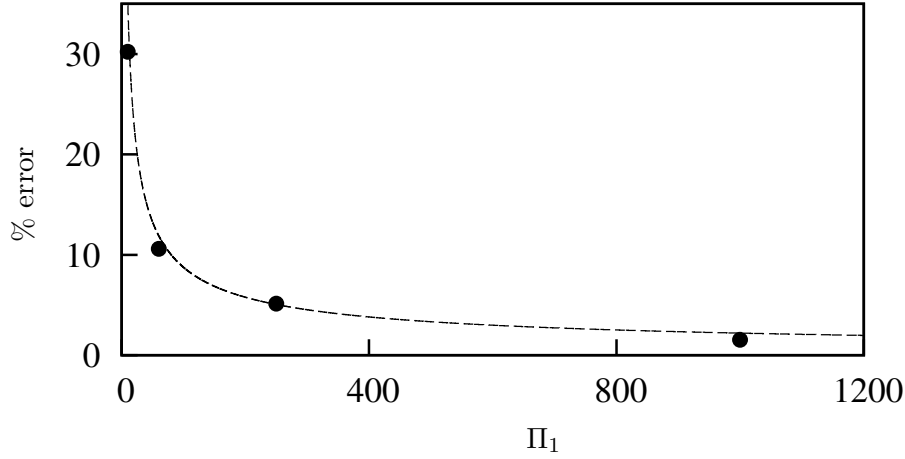
Figure 3.10: The percentage error between the maximum power obtained using DNS data and predicted by QSS model as a function of Π_1. The deviation between them is large for low values of Π_1. The dash curve (---) follows the power law fit of the percentage error which is $\%error = 138.697\Pi_1^{-0.6}$.

A likely reason for this discrepancy at low Π_1 is the influence of the vortex shedding, which is not accounted for in the QSS model. To investigate this further, frequency spectra for the body velocity from DNS cases at varying values of Π_1, at a value of $\Pi_2 = 0.47$ (close to the value at which the mean extracted power is a maximum), have been produced. They are presented, along with the original time histories in figure 3.11.

This figure shows the velocity signals at $\Pi_1 = 0.8$ and $\Pi_2 = 10, 60, 250$ and 1000 and the corresponding spectrum. The spectral data shows a significant frequency component around $fd/U = 0.156$ which can be identified as the vortex shedding frequency. The magnitude of the frequency component at the vortex shedding frequency clearly reduces as Π_1 is increased. This indicates that the influence of vortex shedding is much more prominent at low Π_1, therefore resulting in larger deviations from quasi-steady state results. This builds on the work of Joly et al. (2012), which was conducted at zero damping, that implied that mean extracted power would be influenced by vortex shedding at low mass.

This influence is explicitly shown here. Figure 3.12 plots the relative intensity of the component at the vortex shedding frequency to the component at the galloping or oscillation frequency in the spectra of figure 3.11.

Similar to the discrepancy between the QSS and DNS mean extracted power shown in
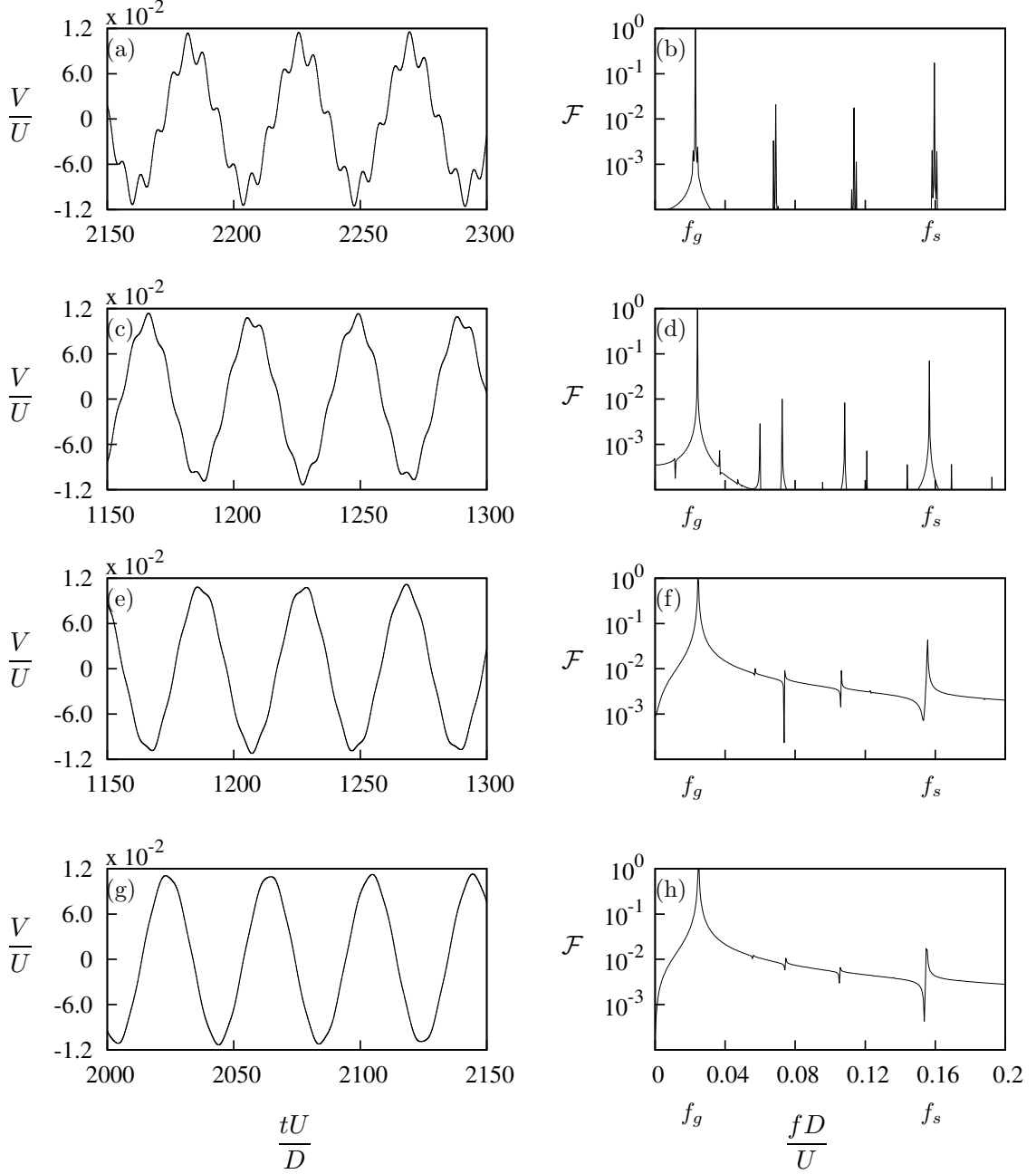
Figure 3.11: Velocity signal (right) and the corresponding power spectrum (left) of the DNS data at four values of Π_1 at $\Pi_2 = 0.47$. (a) and (b) $\Pi_1 = 10$, (c) and (d) $\Pi_1 = 60$, (e) and (f) $\Pi_1 = 250$, (g) and (h) $\Pi_1 = 1000$. f_g and f_s represents galloping and vortex shedding frequencies respectively. U^* is kept at 40 therefore the mass ratio increases as Π_1 increases. It is evident that the influence of vortex shedding reduces as the inertia of the system increases.

Figure 3.12: The relative contribution of the vortex shedding as a function of Π_1. The relative power of the vortex shedding decreases as Π_1 increases. The dash curve (---) follows the power law fit of the percentage error which is Relative power $= 0.977\Pi_1^{-0.52}$.

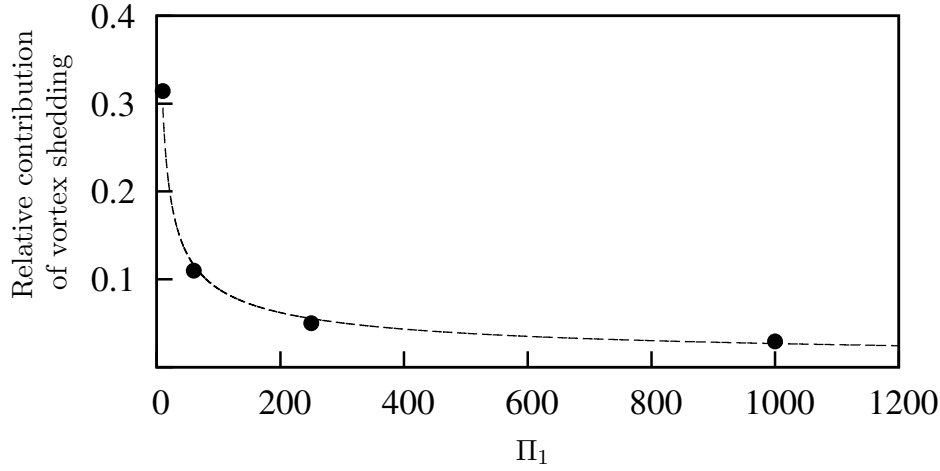figure 3.10, the relative strength of the vortex shedding is seen to be large at small values of Π_1, and quickly decreases as Π_1 is increased. The figure shows that the relative power of the vortex shedding frequency to the galloping frequency varies like $0.977\Pi_1^{-0.52}$.

The difference between the power predicted by the QSS and DNS models scales with $\Pi_1^{-0.6}$; the relative power at the vortex shedding frequency scales with $\Pi_1^{-0.52}$. These scalings are quite similar, and both are close to $1/\sqrt{\Pi_1}$. While not unequivocal, this correlation strongly indicates this discrepancy is due to the influence of the vortex shedding, even though the vortex shedding and galloping frequencies remain separated by around the same amount for all values of Π_1 presented in figure 3.11. The data presented in figure 3.12 also give some indication of the strength of any vortex shedding correction term that might be added to the QSS model in an effort to decrease the discrepancy between it and the DNS simulations.

Further information can be gained by observing the flow field. Non-dimensionalised flow field data at values of Π_2 close to where maximum power is produced at different Π_1 are presented in figure 3.13. The figure shows a clear wavelength of the wake as Π_1 is increased. Qualitatively, this can be interpreted as showing that at high Π_1, the vortex shedding is simply superimposed over the path of motion of the cylinder. It shows a decrease in amplitude of the path of the body at low Π_1, which may be due to the higher levels
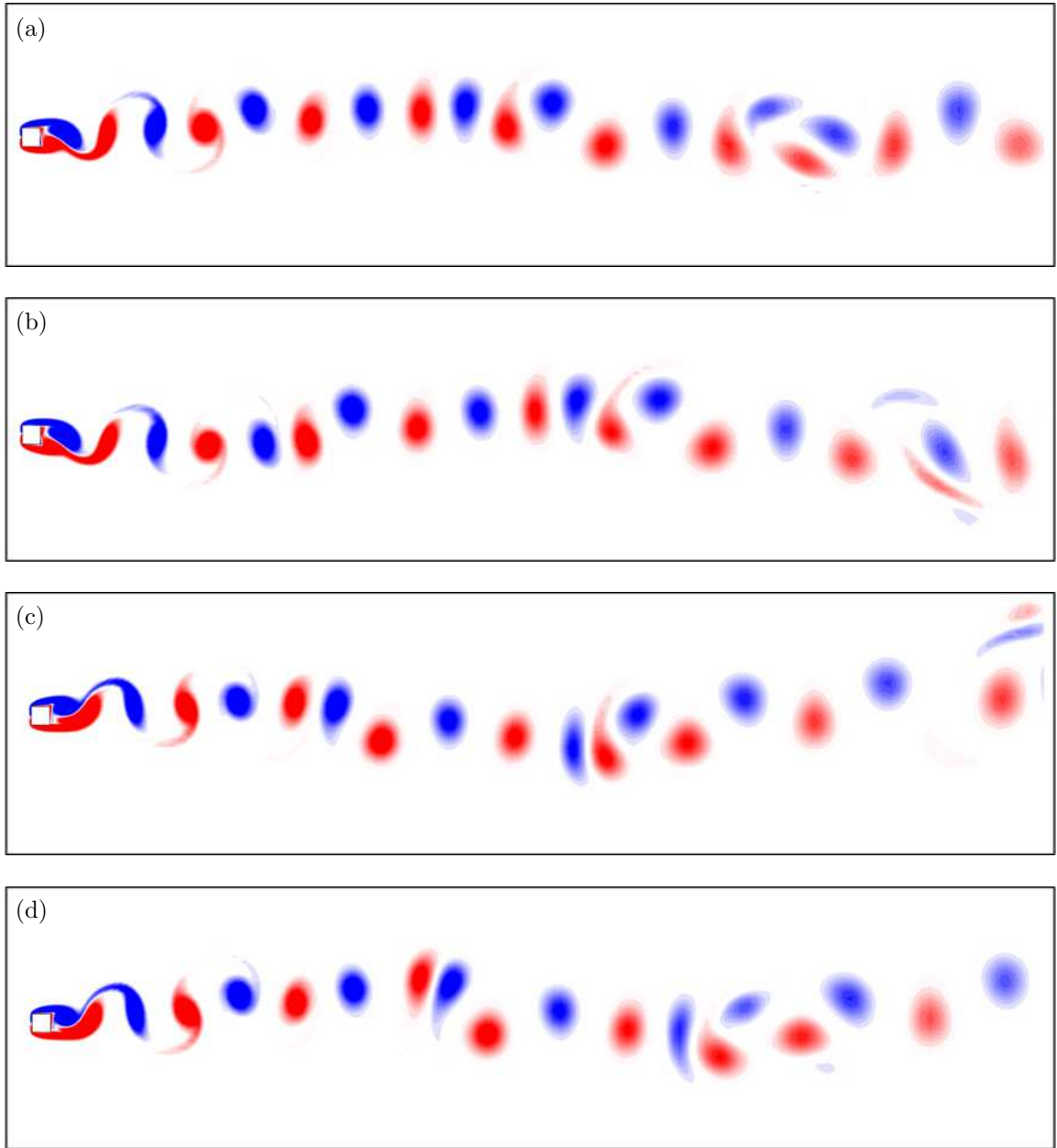
Figure 3.13: Vorticity plots of the flow at arbitrary instants at $\Pi_2 = 0.47$. (a) $\Pi_1 = 10$, (b) $\Pi_1 = 60$ (c) $\Pi_1 = 250$ and (d) $\Pi_1 = 1000$ at $Re = 200$. Contours show vorticity at levels between ± 1.

of non-linear interaction between the vortex shedding and galloping. Such an argument is consistent with the data of figure 3.12 that show the increasing influence of vortex shedding on the velocity of the body as Π_1 decreases. Taken together, this also goes some way to

explaining the discrepancy between the output power predicted by the QSS and DNS models at low Π_1, highlighted in figure 3.10.

3.1 Summary of analysis of power transfer using the QSS model

A need arose after the literature survey to obtain suitable scaling parameters for galloping. These parameters Π_1 and Π_2, were formulated through the natural time-scales of the linearised Quasi-steady state model.

The power transfer of a square body under fluid-elastic galloping was analysed by solving the quasi-steady state oscillator model equation using numerical integration. Power data were presented in terms of both traditional VIV and the newly formulated scaling parameters. A good collapse for predicted output of power could be obtained using the newly formulated dimensionless groups (Π_1, Π_2) in comparison with the classical VIV parameters ,i.e., ζ and U^*. The collapsed data using the dimensionless groups strengthens the argument that the velocity amplitude and the power transfer of the system does not depend on the natural frequency of the system over a large range of natural frequencies.

Even though m^* is an independent parameter as shown in equation 3.8, the results showed that the system is essentially a function of Π_1 and Π_2 only. This seems to be explained by inspection of equation 3.8, which shows that m^* only has an impact on the forcing terms which are non-linear in relation to the body velocity. For these terms to be appreciable, the velocity of the body (and therefore the induced angle of attack) needs to be very high, which appears not to be the case for the range of parameters tested here.

In comparison with the direct numerical simulation data, it could be concluded that the QSS model provides a good estimate of the power output of the system when Π_1 is relatively high. However, at low values of Π_1, the prediction is not close due to the fact that the QSS model does not account for the influence of vortex shedding which is shown to increase as Π_1 is decreased. However, the QSS model does provide a reasonable prediction of the value of Π_2 at which maximum power is produced. Both the error in predicted maximum power between the QSS and the DNS models, and the relative power of the vortex shedding, have been quantified and scale similarly to $1/\sqrt{\Pi_1}$.

CHAPTER 4

_____

OPTIMIZATION OF THE CROSS

SECTION FOR POWER EXTRACTION

4.1 Introduction

Galloping is due to an increase in mean induced lift force C_y with an increase in the instantaneous induced angle of attack. This instantaneous angle of attack is directly related to the transverse velocity - an increase in angle of attack implies an increase in velocity. This increase in mean lift force is created by an increase in the difference in mean pressure on the upper and lower sides of the body. The mean pressure on each side of the body is related to the structure of the mean shear layer, in particular to the separation and potential reattachment of this shear layer, and the size of any resulting recirculation region. An increase in angle of attack forces one shear layer (the lower one figure 1.4) closer to the wall, meaning a high speed region is placed close to this wall. A simple consideration of Bernoulli's equation shows that this high speed region should result in a region of low pressure. This low pressure on the upper side results in a positive pressure difference between the lower and upper sides, and thus a positive mean lift The fact that this mean lift occurs as a function of the angle of attack, and therefore the transverse velocity, implies that this transverse forcing should be in phase with the transverse velocity

From equation 2.2 discussed in section 2.3 it is clear that the power transferred from fluid to the body is a function of the induced forcing F_y and the transverse velocity $\dot{y}$.

The sign of the average power represents the direction of power transfer; positive power represents the power transfer from fluid to the body, negative power represents power transferring from body to the fluid. Thus, according to equation 2.2 it can be deduced that if there is a scenario where both high induced forcing and high transverse velocities are present, higher power output can be achieved.

This can be related directly to the shape of the C_y vs. θ curve. To optimize power transfer this curve should,

- have a high gradient $\partial C_y / \partial \theta$ at $\theta = 0$

- a large maximum C_y

- this maximum C_y should occur at a high value of θ

All of these features can be influenced by the cross section of the body which is galloping. Therefore, if the geometric features of the cross section that influence these curve features can be identified, an informed search for an optimal cross section for power extraction can be undertaken. The major features of the body that influence these C_y vs. θ curve parameters are discussed below.

Luo et al. (1994), showed that the afterbody of the cross section has a direct impact on the C_y vs. θ curve. One interesting observation of this study was that inhibiting the shear layer re-attachment results in a higher peak induced force coefficient C_y occurring at high induced angles (high transverse velocities). The opposite of this result was discussed by Robertson et al. (2003) where long rectangular cross sections did not exhibit galloping due to shear layer reattachment at low θ. Furthermore, Luo et al. (1994) have discussed the impact of the reattachment of the shear layer at the trailing edge. As θ is further increased beyond the angle at which reattachment occurs, the enclosed "bubble" region of the separated reattached shear layer shrinks in size reducing the difference in suction in the top and bottom sides of the body and results in a reduction in C_y (refer section 1.2.3).

Therefore, it can be hypothesised that a higher power transfer could be obtained by inhibiting the shear layer re-attachment.

Here, the influence of the shear layer and its reattachment on the mean power is discussed. It is crucial to keep the shear layer closer to the body for galloping. Thus, a cross

section which has a straight initial section (which has initial streamlining) followed by a slanting section to inhibit the shear, layer had to be considered for analysis. Therefore, a cross section which is a hybrid of a square and a triangle is considered. The cross section is transformed gradually by manipulating the ratio of two length scales. This cross section provide the flexibility of gradually inhibiting the shear layer reattachment while having the initial streamlining of the shear layers to sustain galloping.

The force data are presented for each stationary cross section. This is followed by presentation of extracted power curves, calculate from the QSS model using this force data for each new body. Based on the QSS power data, an optimum cross section for power extraction, from the family of cross sections that have been tested, is identified.

The main features of the generated C_y vs. θ curves for the new bodies are identified and linked to the flow structure present by analysing the mean surface pressure and flow velocity data. Following this, a comparison is made between QSS and DNS mean power on the cross section which provides an optimum mean power.

A final summary is presented outlining that the behaviour of the shear layers is a controlling factor for mean power output. The preliminary design considerations to obtain an optimum power output should therefore focus on the manipulation of these shear layers.

4.2   Influence of the shear layers

In a typical cross section which sustains galloping, the induced lift C_y increases with increasing induced angle θ until it reaches a maximum value of C_y where the shear layer reattachment occurs. The lift force then decreases as θ is further increased. The underlying mechanism for this behaviour is discussed in detail in section 1.2.3.

Selection of the cross section

Several key factors have been considered leading the selection of a suitable cross section for this analysis. These key factors are:

- The cross section should have a bluff front face with sharp upstream corners for the flow to separate at the leading edges;
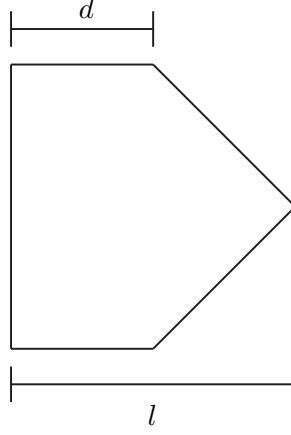
Figure 4.1: Illustration of the hybrid cross section (combination of a square and a triangle) obtained by tapering the afterbody of the square. The afterbody was changed by changing the ratio of $\frac{d}{l}$. Hence, data were obtained for $\frac{d}{l} = 1, 0.75, 0.5, 0.25$ and 0 were considered in this study.

- As the proximity of shear layers to the body plays a vital role in creating C_y (Parkinson, 1989), the cross section should have a basic level of streamlining.

- The cross section should consist of a geometric profile in the afterbody, to inhibit or delay the shear layer reattachment.

The square cross section which is considered as the base cross section in this study satisfies the first two criteria of the selection process. Therefore, in order to inhibit the shear layer reattachment the top and bottom sides of the trailing edges of the square was tapered off and a hybrid cross section of a square and a triangle (illustrated in figure 4.1), i.e, a pentagon was produced. This cross section satisfies all criteria in the cross section selection process. Another advantage of this cross section is the inhibition of the shear layer can be varied systematically by varying one variable which is $\frac{d}{l}$. The $\frac{d}{l}$ was varied gradually from 1 to zero in increments of 0.25 where 1 is the square cross section and 0 is an isosceles triangle.

$\frac{d}{l}$	a_1	a_3	a_5	a_7	
0	-2.30617	-269.075	-59.2929	4.74389	
					$20.5° - 23.5°$
	-5.08342	-56.5390	-160.505	-105.773	
					$28.6° - 28.7°$
	4.40685	19.9213	22.8894	7.68556	
0.25	-0.605146	-19.4346	-82.4463	-94.4226	
					$30.1° - 30.2°$
	2.50538	9.91021	10.2712	3.94112	
0.5	1.44734	4.83885	-166.900e	-983.072	
					$14° - 16°$
	1.51455e	15.8476	52.5465	62.8067	
0.75	1.76938	35.2630	-345.562	-10072.7	
					$11.03° - 11.11°$
	1.77553	43.0120	262.983	638.484	

Table 4.1: Coefficient values used in the 7th order interpolation polynomial at $Re = 200$. Data present for $\frac{d}{l} = 0 - 0.75$ at increments of 0.25. Multiples polynomials were used to attain a better fit. The plot of the compound fit is presented in figure 4.2.

4.3 Static body results

Stationary time averaged C_y results were obtained for cross sections where $\frac{d}{l} = 1, 0.75, 0.5, 0.25$ and 0 using DNS at $Re = 200$. Table 4.1 shows the coefficients of the 7th order curve fitting for each cross section. In order to achieve a better fit, piecewise interpolation using multiple $7th$ order polynomials were incorporated for a single cross section. During the curve fitting process more importance was given to accurately fitting the positive portion of the
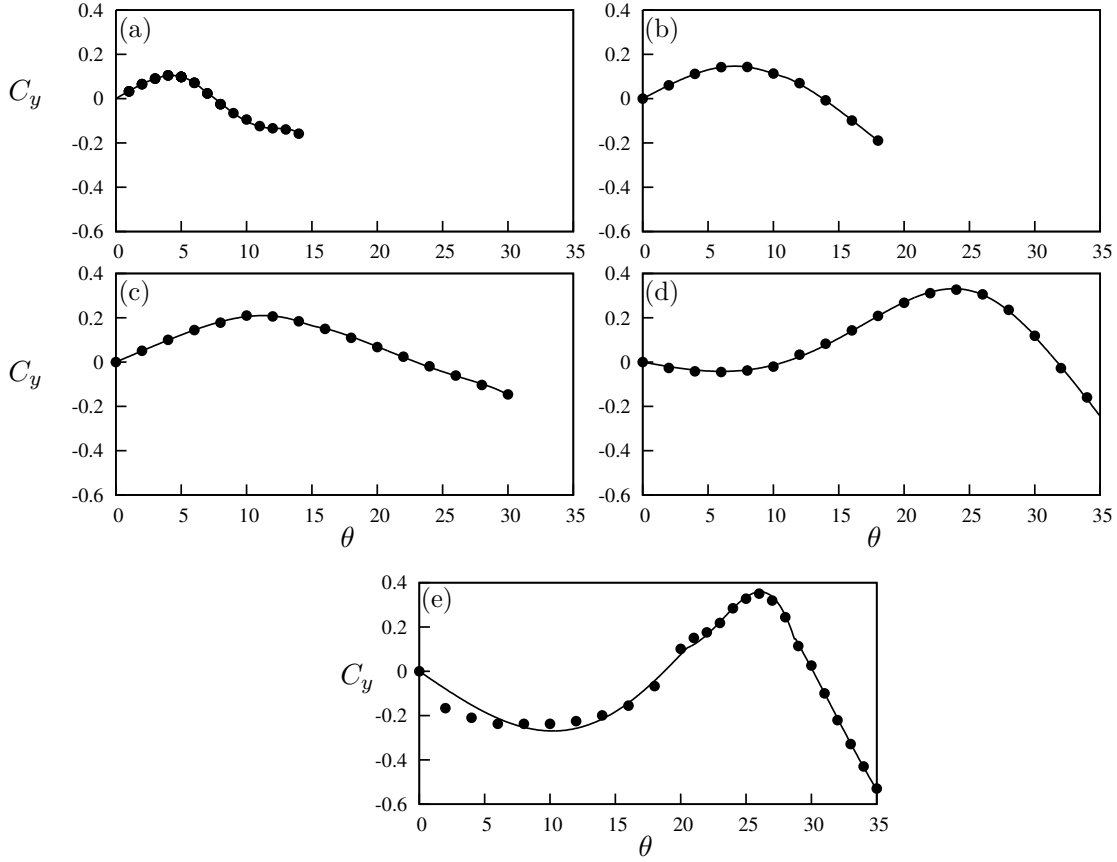
Figure 4.2: Induced lift coefficient C_y at different angles for selected cross sections. Data presented for cross sections, (a) square, (b) $\frac{d}{l} = 0.75$, (c) $\frac{d}{l} = 0.5$, (d) $\frac{d}{l} = 0.25$ and (e) triangle. Points ($\bullet$) are predicted from the static body simulations and the curves are the compound 7th order polynomials.

C_y curve, as the power transfer from the fluid to the body only occurs in this region.

The C_y vs. θ curves in figure 4.2 shows that the peak value of C_y shifts to the right as $\frac{d}{l}$ is increased, hence, the peak C_y occurs at high induced angles. These data agree with Luo et al. (1994) where the peak of the maximum C_y value was shifted to higher induced angles when reattachment was delayed. As θ is proportional to the transverse velocity of the body via $\tan\theta = \frac{\dot{y}}{U}$, the peak value of C_y occurs at high induced velocities as $\frac{d}{l}$ is decreased. Therefore, bodies with a short straight section, or small $\frac{d}{l}$, satisfy one of the three conditions required to optimize the power transfer.

However, a complicating factor is the appearance of a negative region on the C_y vs. θ curves for cross sections where $\frac{d}{l} \leq 0.25$. Here, initially C_y decreases as θ is increased and

only increases after reaching a minimum, nonzero value of θ. The presence of this negative portion is an indication of unfavourable power transfer, i.e. power transferred from body to the fluid as the direction of the force and velocity vectors are out of phase. This implies that when the induced angle of attack is low (when the transverse velocity is low), power transfer is from the body to the fluid, but when the transverse velocity is high, power transfer is from the fluid to the body. This means that the direction of power transfer can be different at different points in the oscillation cycle. This will be further discussed in the upcoming section 4.5.
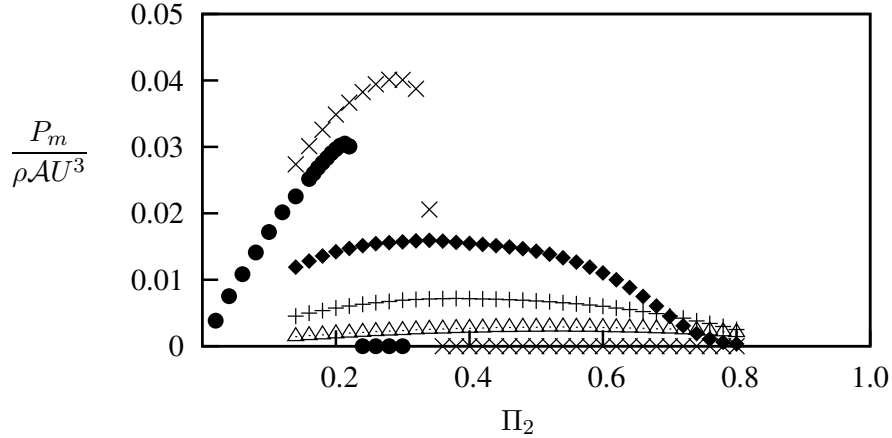
4.4 QSS Mean power output

Figure 4.3: Dimensionless mean power obtained using QSS model as a function of Π_2. Data presented for five selected cross sections, square ($\triangle$), $\frac{d}{l} = 0.75$ (+), $\frac{d}{l} = 0.5$ ($\blacklozenge$), $\frac{d}{l} = 0.25$ ($\times$) and triangle ($\bullet$) at $Re = 200$, $\Pi_1 = 100$.

Mean power output predictions are obtained for these different cross sections using the QSS model and the stationary induced lift data shown in figure 4.2 used as inputs to the QSS model. Figure 4.3 shows the mean power vs. Π_2 for different cross sections namely $\frac{d}{l} = 1, 0.75, 0.5, 0.25$ and 0. The cross sections are divided into two cases, high ($\frac{d}{l} > 0.25$) and low ($\frac{d}{l} \leq 0.25$). The general trends of power follows the trends observed in section 3.0.3 in both cases. The mean power increases peaks and reduces as Π_2 is decreases. At high $\frac{d}{l}$ cases have similar trends where the amount of power increases with a decrease in $\frac{d}{l}$.

For the low $\frac{d}{l}$ cases, the trend is different; power first increases with Π_2, then peaks, and then drops dramatically. The power extracted also appears to decrease with a decrease in $\frac{d}{l}$. Furthermore, negative regions of the C_y vs. θ curves in figure 4.2 in low $\frac{d}{l}$ cases. The change in trends power and C_y in high and low $\frac{d}{l}$ cases clearly indicates that there is a distinct change in the flow structure in these two regions. This fact is further investigated in section 4.5.

4.5 Investigation of flow characteristics at low $\frac{d}{l}$ cases

The analysis of the mean power and the static body results showed that there is a significant change in the flow structure at low $\frac{d}{l}$ cases. As the change in mean C_y is the only input of fluid-dynamics in the QSS model, the distinct features in the C_y vs. θ curves provides an indication of the change in flow structure which results the distinct change in mean power discussed in section 4.4. The main difference between high and low $\frac{d}{l}$ case is the presence of the negative region in C_y vs. θ curves. Thus, it is of interest to investigate the underpinning reason for the negative region in the low $\frac{d}{l}$ cases. The triangle ($rstio = 0$) which produced the largest negative region out of the cross sections considered, is taken as the representative of the low $\frac{d}{l}$ cases for further investigation.

4.5.1 Surface pressure

The driving force of galloping is the induced force F_y created as a result of the freestream velocity of the fluid and the transverse velocity of the body. As discussed in section 1.2.3 the pressure difference of the upper and lower sides of the body (figure 1.4) creates this induced force as a result of the relative proximities of the shear layers to the respective sides. Thus, the primary investigation was carried out analysing surface pressure data on the time averaged stationary data of the cross section.

Time averaged (to filter out the influence of vortex shedding) surface pressure data on the top and bottom surfaces of the cross sections at $\theta = 4°$, $\theta = 16°$ and $\theta = 21°$ were obtained for the isosceles triangle. These angles corresponds to the regions of the C_y vs θ curve of the triangle where the negative C_y increases, negative C_y decreases and a significantly positive value of C_y.
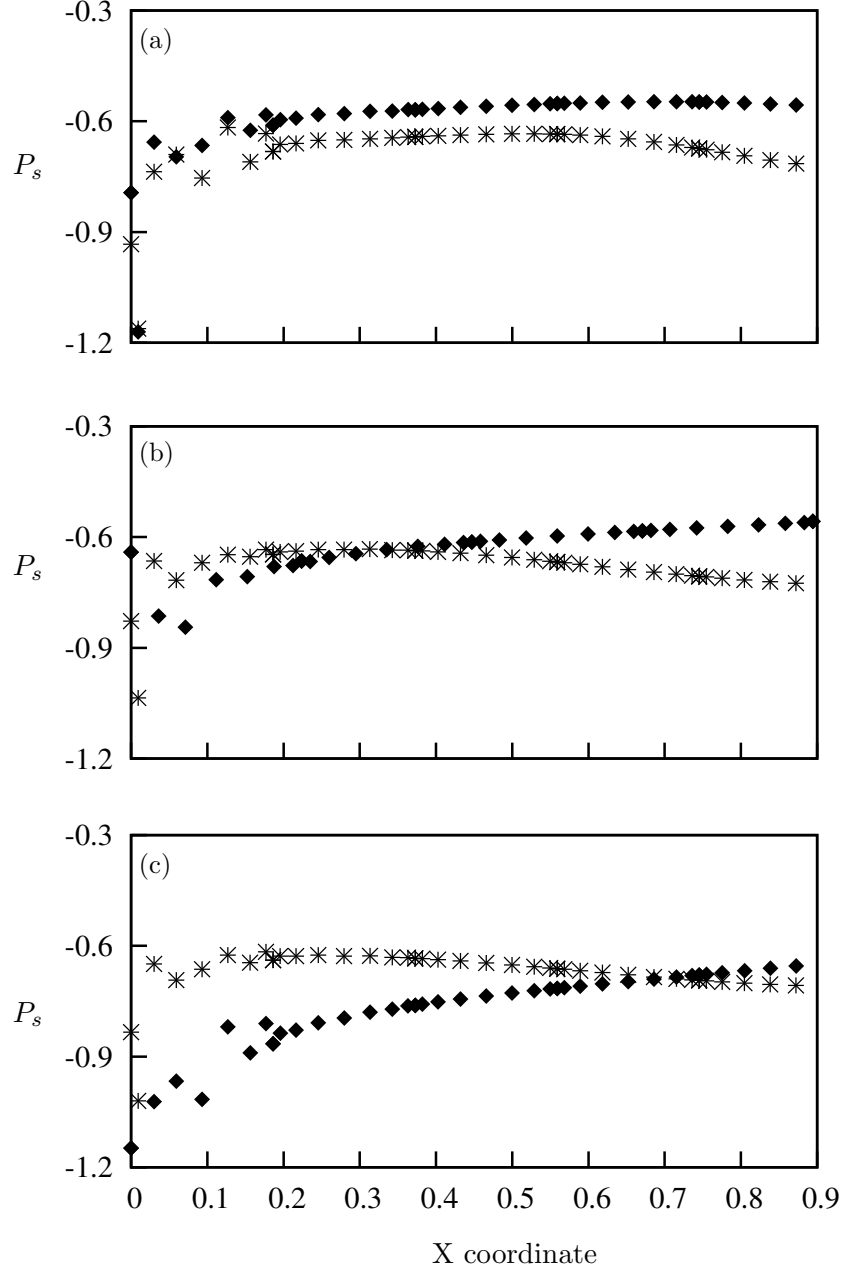
Figure 4.4: Surface pressure of top ($\times$) and bottom ($\blacklozenge$) surfaces of the static triangular cross section at (a) $\theta = 4°$, (b) $\theta = 16°$ and (c) $\theta = 21°$ A clear pressure difference is visible between the surfaces. The top surface comparatively has more negative pressure where a lift is created which results in a negative C_y at $4°$ and reduces as θ is increased, while the vice versa occurs at the top surface.

Figure 4.4 shows the surface pressure of the top and bottom surfaces of the body ($\frac{d}{l} = 0$) as function of the distance from the leading edge. At $\theta = 4°$, the pressure of the bottom of the body is greater than the top. As a result, a pressure difference is created and a force is generated in the upward direction which according to the sign convention in figure 1.1, is against the velocity of the body, hence giving a negative C_y. As θ (figure 4.4 (b)) is increased, to $16°$ the gap between the surface pressure at the leading edge between the top and the bottom reduces. This effect results in a reduction of the magnitude of C_y (although it is still negative). As θ is further increased at $21°$ (figure 4.4 (c)) the surface pressure on the top side becomes greater than the bottom. Therefore, the net effect of the pressure difference is a positive C_y which the driving force F_y in phase with the velocity of the body.

**KJ: Justin I want to write something like this pressure analysis is sort of the stepping stone to analyze the velocity priofiles at the separation points and the shear layer analysis. Because finally we say that there are two mechanisms. One is the bernulli's forcing and the other one is the proximity of the shear layer effect. the former dominates at the negative region because the shear layer which should be closer to the body is not close enough to provide the shear layer effect. I can't word this out can you give me some points ? **

4.5.2 Velocity profiles at the points of flow separation

Like the presence of the afterbody in a cross section, flow separation at the leading edge is vital for galloping as it creates the shear layers which sustains it.

The most important points of a cross section under galloping are the two flow separation points of the leading edges of the cross section, where a significant pressure difference occur JL: a pressure difference between the two separation points? What evidence do you have that these are the "most important" points? Considering all of the discussion so far in this chapter has focussed on reattachment, I would think that the reattachment points are the most important points. A key variable which directly relates to the fluid dynamic pressure is the velocity of the fluid. Although not strictly true in all cases of viscous flows, one should expect that a higher flow speed correspond with a lower pressure from basic fluid dynamic theory. By measuring the flow velocity behaviour at, or near, the separation points, the cause of the pressure differences that occur along the upper and lower surfaces
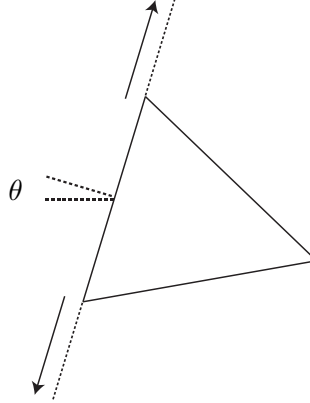
shown in section (SEE ABOVE) can be found.

Figure 4.5: Illustration of the lines along which the flow velocity magnitudes have been extracted. The data have been extracted along a line starting from the separation points in the outward direction (shown with arrows) for the top and bottom surfaces.

Mean velocity magnitude data of the flow were obtained along two lines parallel to the front wall of the cross section one stating at the top and the other stating at the bottom leading edges of the cross section spreading outward as illustrated in figure 4.5. The lengths of these lines were equal to the width of the cross section. Data were obtained for the same cases presented earlier i.e. isosceles triangle ($\frac{d}{l} = 0$) at $\theta = 4°$, $\theta = 16°$ and $\theta = 21°$.

KASUN: Does the velocity go back to zero at 0 distance? Why not show the whole range of V_m?

Also, pick a symbol for the distance rather than writing "Distance from the trailing edge", and show this symbol on the graph and the sketch.

Also, you realise you have used α in the caption of angle of attack, but the rest of your thesis uses θ?

The velocity profiles at the chosen three incident angles are presented in figure 4.6. A sudden rise of velocity magnitude could be observed at the flow separation points JL: at the separation points the velocity is, and must be, zero. I think what your profiles show is the formation of a wall jet. The maximum velocity magnitude in the top wall jet at $\theta = 4^0$ (figure 4.6 (a)) is higher than that in the corresponding bottom wall jet, leading to a lower pressure at the top edge. However, the velocity magnitude in the bottom wall
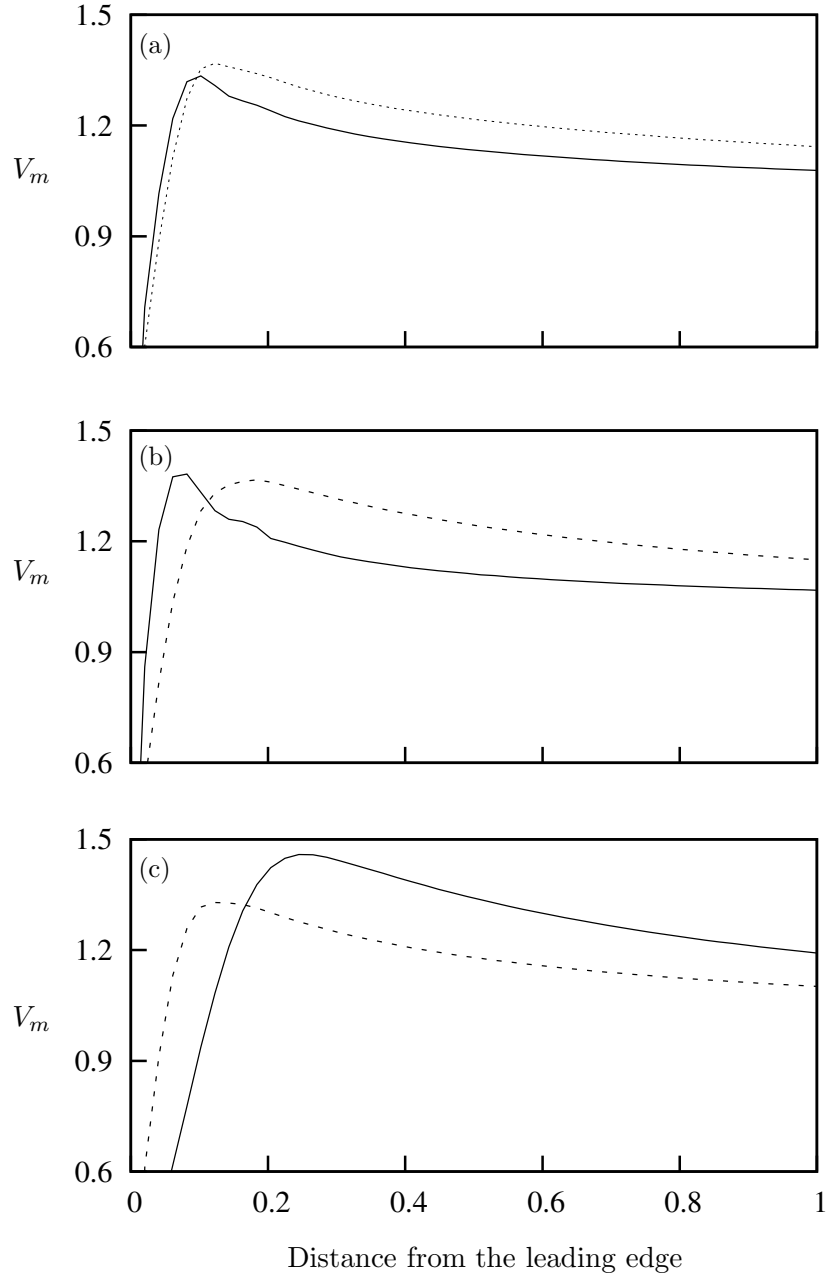
Figure 4.6: Velocity magnitudes of the flow along a line parallel to the front surface spreading towards top (-- -) and bottom (——) boundaries (figure 4.5). These two lines (for the top and bottom surfaces) start from the top and bottom leading edges of the triangular cross section. Data present (a) $\alpha = 4°$, (b) $\alpha = 16°$ and (c) $\alpha = 21°$.
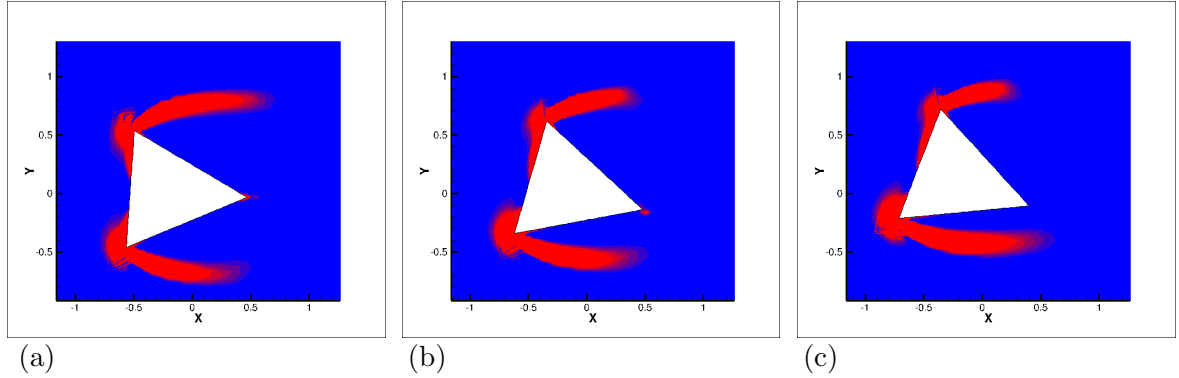
(a)　　　　　　　　(b)　　　　　　　　(c)

Figure 4.7: Contours of the magnitude of the shear strain rate of time averaged flow field on the stationary isosceles triangle ($\frac{d}{l} = 0$) at $Re = 200$ at different incidence angles. (a) $4°$ (negative value of C_y that is further decreasing with increasing θ), (b) $16°$ (negative value of C_y that is increasing with increasing θ) and (c) $21°$ θ and a significantly positive value of C_y. The bottom shear layer comes closer to the bottom wall and as the angle of incidence increases.

jet becomes greater than that in the top wall jet at $\theta = 16°$. The difference between the top and bottom velocity magnitude in these wall jets tends to increase as θ is increased to $21°$, where the velocity magnitude at the bottom is greater than at the top (figure 4.6 (c)). This effectively creates the pressure difference created in figure 4.4 (c), which leads to a positive C_y and results in a forcing which is in phase with the velocity of the body.

KASUN: I am not convinced by this. I can see that the magnitude of the upper jet increases with θ, but the lower one seems almost unaffected. I can also see that the maximum of the upper jet first moves towards the surface, then away again. How does this fit with your basic Bernoulli argument?

Why do you need profiles at all? Why can't you plot contours of velocity magnitude? In fact, you could also replace figure 3.4 with plots of pressure contours. Or keep what you have but add plots of contours. I think this whole section would also be stronger if you contrasted a low $\frac{d}{l}$ case (the triangle) with a high $\frac{d}{l}$ case (the square).

Also, why does the dotted line change format between a and b?

4.5.3 Mean streamlines

The magnitude of the strain rate tensor of the time averaged flow-field of the stationary isosceles triangle at $\theta = 4°$, $\theta = 16°$ and $\theta = 21°$ are presented in figure 4.7. Here, it can be observed that the proximity of the bottom shear layer increases as θ is increased from $4° - 21°$. JL: proximity to what? How do I identify the "shear layer" from the streamlines? Would magnitude of the strain rate tensor be better as it shows shear strain rate (and therefore shear stress) directly

$$\epsilon = \frac{1}{2} \begin{bmatrix} 2\frac{\partial u}{\partial x} & \frac{\partial u}{\partial y} + \frac{\partial v}{\partial x} \\ \frac{\partial v}{\partial x} + \frac{\partial u}{\partial y} & 2\frac{\partial v}{\partial y} \end{bmatrix} \tag{4.1}$$

so

$$|\epsilon| = \frac{1}{2}\left(4\frac{\partial u}{\partial x}\frac{\partial v}{\partial y} + \left(\frac{\partial u}{\partial y} + \frac{\partial v}{\partial x}\right)^2\right) \tag{4.2}$$

By comparing the pressure and the velocity plots together with the stream function flow-field data, it could be seen C_y is governed by two mechanisms. Initially at $\theta = 4°$ an uneven distribution of the flow is created due to the profile and the positioning (angle of attack) of the geometry creating a forcing (F_y) similar to the generation of lift of an aerofoil. Comparing figure 4.7 (a) to (b) and (c) the proximity of the bottom shear layer low and hence, does not create a significant pressure force form the relative proximities of the top and bottom shear layers. Therefore, the aerofoil effect becomes more dominant.

As θ is increased from $\theta = 16°$ to $21°$, the proximity of the bottom shear layer to the wall of the body increases (figure 4.7 (b) and (c)), and thus becoming the more dominant forcing of the system. This uneven flow distribution as discussed earlier and in 1.2.3in detail, creates the positive region of the C_y vs. θ curve.

KASUN: I don't really follow any of this argument. Can you spell it all out in dot points before we go back to writing it? I'm sure there is a logical argument, but you haven't put that argument here.

Bibliography

Alonso, G., Meseguer, J., Pérez-Grande, I., 2005. Galloping instabilities of two-dimensional triangular cross-section bodies. Experiments in Fluids 38, 789–795.

Alonso, G., Meseguer, J., Sanz-Andrés, A., Valero, E., 2010. On the galloping instability of two-dimensional bodies having elliptical cross-sections. Journal of Wind Engineering and Industrial Aerodynamics 38, 789–795.

Alonso, G., Valero, E., Meseguer, J., 2009. An analysis on the dependence on cross section geometry of galloping stability of two-dimensional bodies having either biconvex or rhomboidal cross sections. European Journal of Mechanics B/Fluids 28, 328–334.

Barrero-Gil, A., Alonso, G., Sanz-Andres, A., Jul. 2010. Energy harvesting from transverse galloping. Journal of Sound and Vibration 329 (14), 2873–2883.

Barrero-Gil, A., Sanz-Andrés, A., Roura, M., Oct. 2009. Transverse galloping at low Reynolds numbers. Journal of Fluids and Structures 25 (7), 1236–1242.

Bearman, P. W., Gartshore, I. S., Maull, D. J., Parkinson, G. V., 1987. Experiments on f low-induced vibration of a square-section cylinder. Journal of Fluids and Structures 1, 19–34.

Bernitsas, M. M., Ben-Simon, Y., Raghavan, K., Garcia, E. M. H., 2009. The VIVACE Converter: Model Tests at High Damping and Reynolds Number Around 10[sup 5]. Journal of Offshore Mechanics and Arctic Engineering 131 (1), 011102.

Bernitsas, M. M., Raghavan, K., Ben-Simon, Y., Garcia, E. M. H., 2008. VIVACE (Vortex Induced Vibration Aquatic Clean Energy): A new concept in generation of clean and

renewable energy from fluid flow. Journal of Offshore Mechanics and Arctic Engineering 130 (4), 041101–15.

Blevins, R. D., 1990. Flow-Induced Vibration, 2nd Edition. New York: Van Nostrand Reinhold.

Bouclin, D. N., 1977. Hydroelastic oscillations of square cylinders. Master's thesis, University of British Columbia.

Den Hartog, J. P., 1956. Mechanical Vibrations. Dover Books on Engineering. Dover Publications.

Deniz, S. amd Staubli, T., 1997. Oscillating rectangular and octagonal profiles: Interaction of leading-and trailing-edge vortex formation. Journal of Fluids and Structures 11, 3–31.

Fletcher, C. A. J., 1984. Computational Galerkin methods. Springer-Verlag, New York.

Fletcher, C. A. J., 1991. Computational techniques for fluid dynamics. Vol. 1. Springer-Verlag, New York. Gabbai,.

Glauert, H., 1919. The rotation of an aerofoil about a fixed axis. Tech. rep., Advisory Committee on Aeronautics R and M 595. HMSO, London.

Griffith, M. D., Leontini, J. S., Thompson, M. C., Hourigan, K., 2011. Vortex shedding and three-dimensional behaviour of flow past a cylinder confined in a channel. Journal of Fluids and Structures 27 (5-6), 855–860.

Joly, A., Etienne, S., Pelletier, D., Jan. 2012. Galloping of square cylinders in cross-flow at low Reynolds numbers. Journal of Fluids and Structures 28, 232–243.

Karniadakis, G. E., Sherwin, S., 2005. Spectral/hp element methods for computational fluid dynamics, ii Edition. Oxford University.

Kreyszig, E., 2010. Advanced Engineering Mathematics, 10th Edition. John Wiley & Sons.

Lee, J., Bernitsas, M., Nov. 2011. High-damping, high-Reynolds VIV tests for energy harnessing using the VIVACE converter. Ocean Engineering 38 (16), 1697–1712.

Lee, J., Xiros, N., Bernitsas, M., Apr. 2011. Virtual damperspring system for VIV experiments and hydrokinetic energy conversion. Ocean Engineering 38 (5-6), 732–747.

Leonard, A., Roshko, A., 2001. Aspects of flow-induced vibrations. Journal of Fluids and Structures 15, 415–425.

Leontini, J. S., 2007. A numerical investigation of transversely-oscillating cylinders in two-dimensional flow. Ph.D. thesis, Monash University.

Leontini, J. S., Lo Jacono, D., Thompson, M. C., Nov. 2011. A numerical study of an inline oscillating cylinder in a free stream. Journal of Fluid Mechanics 688, 551–568.

Leontini, J. S., Thompson, M. C., 2013. Vortex-induced vibrations of a diamond cross-section: Sensitivity to corner sharpness. Journal of Fluids and Structures 39, 371–390.

Leontini, J. S., Thompson, M. C., Hourigan, K., Apr. 2007. Three-dimensional transition in the wake of a transversely oscillating cylinder. Journal of Fluid Mechanics 577, 79.

Luo, S., Chew, Y., Ng, Y., Aug. 2003. Hysteresis phenomenon in the galloping oscillation of a square cylinder. Journal of Fluids and Structures 18 (1), 103–118.

Luo, S. C., Yazdani, M., Chew, Y. T., Lee, T. S., 1994. Effects of incidence and afterbody shape on flow past bluff cylinders. Journal of Wind Engineering 53, 375–399.

Nakamura, Y., Mizota, T., 1975. Unsteady lifts and wakes of oscillating rectangular prisms. ASCE Journal of the Engineering Mechanics Division 101, 855–871.

Nakamura, Y., Tomonari, Y., 1977. Galloping of rectangular prisms in a smooth and in a turbulent flow. Journal of Sound and Vibration 52, 233–241.

Naudascher, E., Rockwell, D., 1994. Flow-induced vibrations: An engineering guide. A.A. Balkema, Rotterdam.

Naudascher, E., Wang, Y., 1993. Flow induced vibrations of prismatic bodies and grids of prisms. Journal of fluids and structures 7, 341–373.

Ng, Y., Luo, S., Chew, Y., Jan. 2005. On using high-order polynomial curve fits in the quasi-steady theory for square-cylinder galloping. Journal of Fluids and Structures 20 (1), 141–146.

Païdoussis, M., Price, S., de Langre, E., 2010. Fluid-Structure Interactions : Cross-Flow-Induced Instabilities. Cambridge University Press.

Parkinson, G., 1989. Phenomena and modelling of flow-induced vibrations of bluff bodies. Progress in Aerospace Sciences 26, 169–224.

Parkinson, G., Brooks, N. P. H., 1961. On the aeroelastic instability of bluff cylinders. Journal of Applied Mechanics 28, 252–258.

Parkinson, G. V., 1974. Mathematical models of flow-induced vibrations of bluff bodies. In Flow-Induced Structural Vibrations, e. naudascher Edition. Berlin: SpringerVerlag.

Parkinson, G. V., Smith, J. D., 1964. The square prism as an aeroelastic non-linear oscillator. The Quarterly Journal of Mechanics and Applied Mathematics 17 (2), 225–239.

Pregnalato, C., 2003. Flow-induced vibrations of a tethered sphere. Ph.D. thesis, Monash University.

Raghavan, K., Bernitsas, M., Apr. 2011. Experimental investigation of Reynolds number effect on vortex induced vibration of rigid circular cylinder on elastic supports. Ocean Engineering 38 (5-6), 719–731.

Raghavan, K., Bernitsas, M. M., Maroulis, D. E., 2009. Effect of Bottom Boundary on VIV for Energy Harnessing at $8 \times 10^3 < Re < 1.5 \times 10^5$. Journal of Offshore Mechanics and Arctic Engineering 131 (3), 031102.

Robertson, I., Li, L., Sherwin, S. J., Bearman, P. W., 2003. A numerical study of rotational and transverse galloping rectangular bodies. Journal of Fluids and Structures 17, 681 – 699.

Ruscheweyh, H., Hortmanns, M., Schnakenberg, C., 1996. Vortex-excited vibrations and galloping of slender elements. Journal of Wind Egineering and Industrial Aerodynamics 65, 347–352.

Sheard, G. J., Fitxgerald, M. J., Ryan, K., Jun. 2009. Cylinders with square cross-section: wake instabilities with incidence angle variation. Journal of Fluid Mechanics 630, 43.

Shiels, D., Leonard, A., Roshko, A., 2001. Flow-induced vibration of a circular cylinder at limiting structural parameters. Journal of Fluids and Structures 15, 3–21.

Thompson, M., Hourigan, K., Sheridan, J., Feb. 1996. Three-dimensional instabilities in the wake of a circular cylinder. Experimental Thermal and Fluid Science 12 (2), 190–196.

Thompson, M. C., Hourigan, K., Cheung, A., Leweke, T., Nov. 2006. Hydrodynamics of a particle impact on a wall. Applied Mathematical Modelling 30 (11), 1356–1369.

Tong, X., Luo, S., Khoo, B., Oct. 2008. Transition phenomena in the wake of an inclined square cylinder. Journal of Fluids and Structures 24 (7), 994–1005.

Tu, J., Yeoh, G., Liu, C., 2008. Computational Fluid Dynamics: A Practical Approach, 1st Edition. Butterworth-Heinemann.

Vicente-Ludlam, D., Barrero-Gil, A., Velazquez, A., 2014. Optimal electromagnetic energy extraction from transverse galloping. Journal of Fluids and Structures 51, 281–291.

Vio, G., Dimitriadis, G., Cooper, J., Oct. 2007. Bifurcation analysis and limit cycle oscillation amplitude prediction methods applied to the aeroelastic galloping problem. Journal of Fluids and Structures 23 (7), 983–1011.

Weaver, D. S., Veljkovic, I., 2005. Vortex shedding and galloping of open semi-circular and parabolic cylinders in cross-flow. Journal of Fluids and Structures 21, 65–74.

White, F., 1999. Fluid mechanics, 4th Edition. McGraw-Hill, Boston.

Williamson, C. H. K., Govardhan, R., 2004. Vortex-induced vibrations. Annual Review of Fluid Mechanics 36, 413–455.